PROCEEDINGS, 48th Workshop on Geothermal Reservoir Engineering
Stanford University, Stanford, California, February 6-8, 2023
SGP-TR-224

Modeling and Analysis of Hybrid Geothermal-Solar Energy Storage Systems in Arizona

Moones Alamooti[1,2], Olusegun Stanley Tomomewo[2], Ajan Meenakshisundaram[2], Jerjes Porlles Hurtado[2], Etochukwu Uzuegbu[2], Emmanuel Gyimah[2]

Harold Hamm School of Geology & Geological Engineering, University of North Dakota, Grand Forks 58202, USA [1]

Institute of Energy Studies, University of North Dakota, Grand Forks 58202, USA [2]

moones.alamooti@und.edu ; olusegun.tomomewo@und.edu ; a.meenakshisundaram@und.edu ; j.porlleshurtado@und.edu ; e.uzuegbu@und.edu ; emmanuel.gyimah@und.edu

Keywords: Hybrid Systems, Hybrid Solar-Geothermal Systems, Renewable Energy, Systems Optimization, Geothermal Resources, High Efficiency, Electricity, Systems Integration

ABSTRACT

Intermittency, low-capacity factor, and grid instability are key factors preventing renewable energy from being cost-competitive with conventional energy resources in all locations. This is unfortunate since renewable energy has many promising environmental and sustainability benefits. Particularly, solar-geothermal hybrids (including photovoltaic and concentrated solar power) have been shown to be a favorable and auspicious combination of renewable energy sources. Integrating geothermal and solar energy is feasible since regions have high geothermal heat flow and surface radiation. The efficiency of power generation from geothermal energy is related to the resource temperature, which is why the geothermal business prioritizes geothermal resources with high temperatures. Most geothermal resources only reach temperatures of approximately 150 °C, a low- moderate temperature. The alternative is to utilize solar energy to heat geothermal fluids, which would boost the efficiency of geothermal power plants. Geothermal fluids have the potential to act as storage systems for solar energy. This ability leads to overcoming several issues in solar energy systems, including reliance on the weather and volatility. In addition, if concentrated solar powers (CSPs) are integrated into a geothermal power plant, they may be able to meet the peak power demand throughout the day, which is helpful for the lifespan of geothermal fields. In the United States, some of Arizona's hot springs are found in the state's southeastern section, the Clifton area, which might be harnessed to generate electricity.

On the other hand, Arizona is one of the sunniest states and has enormous potential to grow in the solar industry. In this article, we discuss the possibility of developing solar and geothermal power systems in Arizona. Then, we evaluate stand-alone solar and geothermal power plants in Arizona to make a comparison between different energy storage systems. Finally, we analyze the stand-alone efficiency, hybrid efficiency, and the percentage of incremental efficiency from the literature. We use Engineering Equation Solver (EES) to analyze the system's performance and estimate the energy cost. This model's results will help us evaluate the designs, methods, and distinctive characteristics of creating hybrid solar-geothermal power plants in Arizona. The conclusion is that integrating geothermal and solar energy systems will boost the system efficiency and power output of both energy sources and provide a promising new avenue for research and development in Arizona State.

1. INTRODUCTION

It is common knowledge that industrial-era energy output has been at odds with climatic stability. The problem will only worsen as the global population grows unless something is done to improve how energy demands are fulfilled. The United Nations projects that by 2030, the world's population will exceed 8.5 billion, and by 2050 it will have risen to 9.7 billion; after reaching 10.4 billion in the years 2070–2100, growth is predicted to slow (UNDESA, 2019). The population will instead reach its highest point of 9.3 billion in 2064, according to research by Vollset et al. (2020). However, even moderate expansion would put a considerable demand on all available resources. In order to provide for the energy demands of such a large and rising population, it is necessary to investigate any potential energy sources. The well-known goals of the Paris Agreement are lofty; they include limiting the increase in Earth's temperature to 1.5°C by 2050 over preindustrial levels and achieving net-zero emissions in the later part of the 21st century. Though only 51 of the 193 signatories have long-term plans, these objectives may be partly met via proactive policymaking (Climate Watch, 2022). Still, steady progress in renewable energy technology is crucial. That is why there has been a substantial and well-documented increase in the global renewable sector in recent years. Qi et al. (2022) cited a rise in worldwide renewable energy usage from 2010 to 2020, from 9.63 to 31.71 EJ. However, the intermittent nature of many green power sources presents a significant problem, making the integration of suitable storage all the more critical. It is essential to take a quick look at the different hybrid system storage solutions available.

It has been, and will continue to be, very difficult to provide a reasonably affordable, adequate, and sustainable source of clean energy. Due to factors like market penetration, abundance, and the ability to give either base-load (geothermal) or distribution (wind and solar) power, wind, geothermal, and solar energy are among the most feasible contemporary renewable energies (Li et al., 2015; Zhou et al., 2013). However, as highlighted by Li et al. (2015) and many others, geothermal and solar energy have advantages and disadvantages (Zhou et al., 2013). Geothermal energy systems, for instance, have the burden of requiring relatively high temperatures to create electricity but the benefit of being a base-load system unaffected by weather. In the meantime, CSP (concentrated solar power) systems may reach high temperatures exceeding 350°C during the day with the aid of a parabolic trough or other technologies, despite dropping to extremely low temperatures at night or when the sun is not shining. We will discuss more how the synergy between the two

renewables may help mitigate their drawbacks in the coming parts. One of the most pressing concerns is choosing the most effective hybridization of CSP and geothermal power-generating technologies to maximize efficiency. There has been a flurry of publications in recent years devoted to the topic of geothermal-solar energy hybrids. However, there has been a shortage of commentary on this topic. This article aims to do just that by delving into a case study of a hybrid plant that combines solar and geothermal energy generating. The primary need of this hybrid energy storage project is solar energy production, followed by scalable storage with geographic flexibility. Using CSP solar is a no-brainer. The hot geothermal fluid in a binary geothermal power plant is routed through a heat exchanger (vaporizer)—a secondary fluid with a low boiling point and high vapor pressure flow to produce electricity. Geothermal fluid and secondary fluid undergo heat exchange, vaporizing the secondary fluid, which drives the turbine, generating energy. Our research shows that the best places for hybrid systems in the United States are in the South, with the location of the solar resource playing the most crucial role.

2. LITERATURE REVIEW

2.1 Arizona State Energy Profile

From the Grand Canyon in the north to the Saguaro deserts in the South, Arizona is home to a wide variety of breathtaking landscapes and natural marvels (Arizona (U.S. National Park Service),2022). While fossil fuel supplies are few, the state makes up for them with abundant renewable energy sources (Arizona Profile, 2022). Most of Arizona is semiarid or arid, with some of the nation's most significant solar energy resources due to the abundant sunlight and relatively low average annual temperatures (Selover,2022). Peaks in Arizona's north reach over 12,000 feet in elevation, while the state's southwest deserts are virtually at sea level. The southern end of the Colorado Plateau is marked by the 200-mile-long Mogollon Rim, which runs diagonally across central Arizona from northwest to southeast and has some of the highest altitudes and most enormous wind potential in the state (WINDExchange: Wind Energy in Arizona, 2022). Arizona is home to the most extensive ponderosa pine forest in the United States, among other biomass resources (Arizona Geography From NETSTATE, 2022).

Arizona's overall per capita energy consumption is the sixth lowest in the United States since many of the state's key economic activities are not energy-demanding (U.S. EIA, State Energy Data System, 2019). Moreover, a third of Arizona's energy consumption comes from the transportation sector, while another quarter comes from the residential sector (U.S. EIA, State Energy Data System, 2019). Most Arizonans concentrate in a few big cities, leaving the rest of the state sparsely populated (U.S. Census Bureau, 2010). In 2021, Arizona's year-round population rose faster than in all but three other states due to the state's favorable climate, which has pleasant summers in the north and moderate winters in the South (Schwarz,2021). Many people only stay in their Arizona homes during winter because of the mild winters (U.S. Census Bureau, 2019). Moreover, 20% of all energy used in Arizona is by the business sector, with the industrial sector accounting for around 17% (U.S. EIA, State Energy Data System, 2019).

In 2021, around 16% of Arizona's total net power came from renewable energy generated by utility- and small-scale (less than 1 megawatt) projects. Solar photovoltaic (P.V.) and solar thermal energy accounted for over three-fifths of that sum. Almost the remainder came from hydroelectric power and wind energy. Although conventional hydroelectric power has historically accounted for most of Arizona's renewable energy, utility, and small-scale solar-powered installations contributed more electricity to the state's grid in 2017. About 9% of the state's total net power production in 2021 came from solar energy, most of which came from distributed photovoltaic systems (PVs) installed on buildings' rooftops. 51 In terms of total solar energy potential, Arizona is second only to Nevada; in 2021, the state ranked fifth behind only California, Texas, Florida, and North Carolina in net solar generation (U.S. EIA, Electric Power Monthly, 2022). In addition to being one of just four states where energy is produced using utility-scale solar thermal technology-concentrate sunlight to heat the fluids needed to drive the turbines-Arizona is a leader in this field (U.S. EIA, Electric Power Monthly, 2022). The state of Arizona has just one solar thermal power plant, and it is located in Maricopa County at the Solana Generating Station. Almost 300 megawatts can be produced by it. This solar P.V. plant is not just the biggest in California but also one of the largest in the United States. In Yuma County, Agua Caliente Power Plant can produce over 350 MW(Leonard, 2023). With more than 4,780 MW of solar generating capacity from utility and residential installations, Arizona is among the top five states in the U.S. (U.S. EIA, Electric Power Monthly, 2022).

The state has access to deep, high-temperature geothermal deposits, particularly in southeast Arizona. Although they would be conducive to electricity production, there are currently no geothermal power facilities of any significant size operating in Arizona. The state's geothermal resources are used in various direct-use industries, such as the thriving aquaculture sector, where shrimp and fish are grown. Numerous hot springs and a few spas may be found around the state (U.S. EIA, Electricity Data Browser, 2021).

In 2006, Arizona became one of the states to implement a renewable energy standard (RES). Electric utilities subject to government regulation must obtain at least 15% of their retail energy sales from renewable resources by 2025(Arizona Corporation Commission, 2022). Non-utility, customer-sited generation is responsible for 30% of the annual needed renewable energy goal, split evenly between residential and commercial installations (N.C. Clean Energy Technology Center,2018). Customers in the state may get minor credits on their energy bills for any electricity they create over what they use. This policy is known as "net billing." It supports distributed, renewable generating at the customer's location (N.C. Clean Energy Technology Center,2021). The state's major utility in Arizona declared in 2020 that it aims to provide 100% carbon-free energy, including nuclear power, by 2050, with an intermediate goal of 45% from renewable resources by 2030 (Walton, 2020).

Nevertheless, another major Arizona utility anticipates generating more than 70% of its electricity needs from renewable sources like wind and solar by 2035 (Tucson Electric Power, 2021). Investor-owned utilities, electric cooperatives, and natural gas utilities in Arizona were all mandated to improve their energy efficiency and reduce their power and gas use under a 2010 energy efficiency

standard (EES) N.C. Clean Energy Technology Center,2017). In early 2022, the Arizona Corporation Commission voted against a 100% renewable energy plan that included a 10-year extension of the EES (Ryan Randazzo, The Arizona Republic, 2022).

2.1.1 Solar Energy

Different parameters contribute to Arizona's enormous potential for solar power development, according to the report Renewable Energy Standards (RES): 1)the vast amount of land that is available, 2) the state's abundant solar radiation resources, 3) the state's intention to speed up the development of renewable energy through incentives and ACC-mandated all.

Due to the state's plentiful solar radiation and bright weather, Arizona's Levelized cost of solar energy is significantly lower than in most other U.S. regions. Arizona has the land and water resources to support the quantity of solar production necessary to satisfy the RES criteria for the next 20 years (Frisvold, 2009).

The amount of solar energy produced annually will rise significantly, from 32,300 MWh in 2010 to 9,544,100 MWh in 2030 (Table .1). To achieve this production level, 4,340 MW of solar power capacity must be built by 2030. Solar energy will supply all additional renewable energy needs from 2025 through 2030. (EIA, 2022)

Table 1. Annual utility-scale solar electricity generation (EIA, 2022)

Year	Generation (GWh)	Generation (% of AZ total)	Generation (% of U.S. Solar)
2010	16	<0.1%	1.3%
2011	83	0.1%	4.6%
2012	955	0.9%	22.1%
2013	2,111	1.9%	23.4%
2014	3,142	2.8%	16.9%
2015	3,457	3.1%	13.9%
2016	3,766	3.5%	10.4%
2017	4,942	4.7%	9.3%
2018	5,171	4.6%	7.8%
2019		6.6%	

Phoenix's average monthly Global Horizontal Irradiance (GHI) is 5.78 kWh/m2/day, or about 21% less than the city's average monthly Direct Normal Irradiance (DNI), which is 7.35 kWh/m2/day. Phoenix, Arizona, experiences a yearly average of 6.59-kilowatt hours per square meter per day (kWh/m2/day) of solar radiation. Average Tilt at Latitude, or ATaL, or solar systems in Phoenix that is always titled at Phoenix's latitude, average 6.68 kWh/m2/day, which is about 16% more than the average monthly GHI of 5.78 kWh/m2/day and about 9% less than the average monthly DNI of 7.35 kWh/m2/day (Figure 1). Arizona has an average of 300+ days of sunlight (EIA,2022).

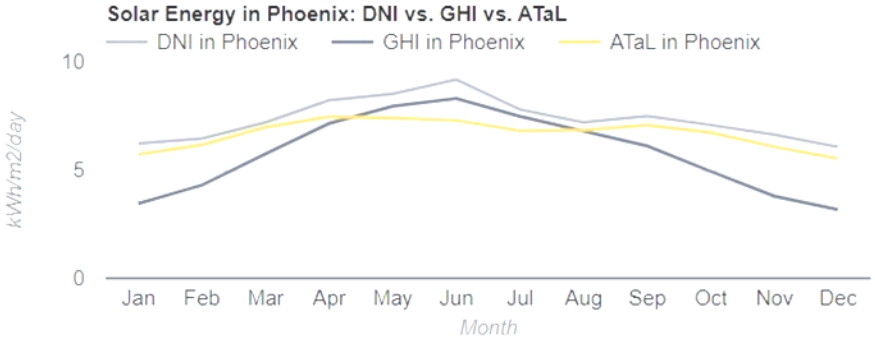

Figure 1. Solar energy in Phoenix, AZ (EIA, 2022)

- Global horizontal irradiance: The total quantity of solar radiation that a constantly horizontally positioned surface receives per unit area.
- Direct normal irradiance: A surface constantly perpendicular to the sun's rays that go directly in a line from the sun at its current location in the sky will receive an equal quantity of solar energy per unit area.
- Average tilt: the total quantity of solar energy a surface slanted toward the equator at an angle equal to the present latitude receives per square meter of surface area. Frequently, ATaL will result in the highest energy production.

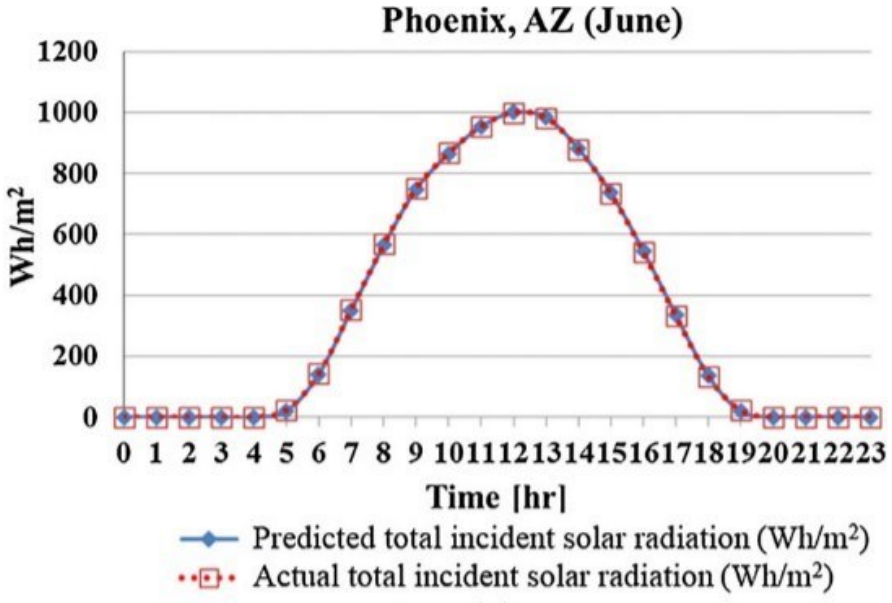

Figure 2.Hourly solar irradiance of Arizona (Abdelhamid, 2016)

Arizona also has the most sunlight compared to any other state. Arizonan solar panels generate roughly 70% more energy than those in places like New York (Figure 2). A high solar output indicates that fewer solar panels are required to produce the specified output (Abdelhamid 2016). Arizona has the capacity to create more than 320 times as much electricity from solar P.V. and concentrating solar power (CSP) plants as the state uses each year. Every one of the 50 states can produce far more power from the sun than its citizens need. Phoenix is the sunniest major city in the United States, averaging 211 clear days yearly. With 3,872 hours of sunshine, solar companies in Phoenix have their work cut out for them. Solar panels in Phoenix can be more efficient than in any other major city with 85% sunshine. The shade trees that may hang over the roof are also a factor in deciding where to put new solar panels. If there is too much shade, we may consider removing some trees to maximize the effectiveness of the solar panels.

2.1.2 Geothermal Energy

Solar power is often the first renewable resource that comes to mind when Arizonans consider their energy needs. Arizona indeed has one of the best solar potentials in the U.S. Arizona, however, has vast quantities of renewable geothermal resources that may be used for farming, manufacturing, heating buildings, and even powering electricity generating stations. Numerous Arizona commercial enterprises have taken advantage of the state's geothermal resources for space heating, aquaculture, and recreational purposes. Arizonans acquire their renewable energy from California's geothermal power plants since the state has no such facilities of its own. Geothermal potential in Arizona has been examined, mainly at the reconnaissance level (both for direct thermal applications and power generation). The Arizona Geological Survey (AZGS), formerly known as the Arizona Bureau of Geology and Mineral Technology, surveyed the state's geothermal resources between 1977 and 1982, emphasizing the southeastern region. Above 1,250 thermal wells and springs with temperatures over 68 degrees Fahrenheit (20 degrees Celsius) were documented in a 1995 database (see Figure 3), while another 215 thermal wells reached temperatures of over 100 degrees Fahrenheit (38 degrees Celsius). Bottom-hole temperature (BHT) values collected during geophysical logging of oil and gas exploration wells or from academic heat-flow studies are among the resources shown on the 1982 map (Figure 3). After completing the survey, the agency released assessments evaluating the potential of Arizona's geothermal resources. The next phase would have been to conduct exploration drilling in the most promising resource regions. Unfortunately, no funding was made available at the federal, state, or industry levels to back the projects as the globe entered an oil glut in 1982, which finally led to a market collapse in 19863. Since these first evaluations were conducted about 25 years ago, technology has advanced, conventional energy costs have skyrocketed, and the state's population has more than doubled. Researchers claim that these variables have stimulated further investigation into the geothermal resource potential of Arizona (Fleischmann, 2006).

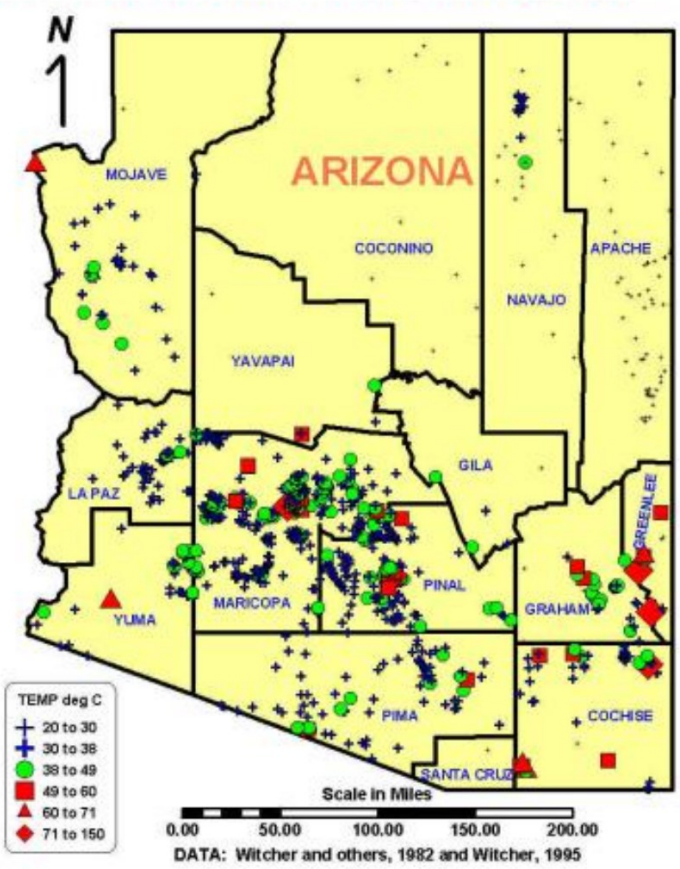

Figure 3. Thermal wells and springs in Arizona (Witcher,1982)

2.2 Hybrid Solar-Geothermal Systems

As was said before, geothermal and solar energy both have advantages and disadvantages (Li et al., 2015; Zhou et al., 2013). Because of the mutual compensation in energy properties and structures, a solar-geothermal hybrid power plant may perform better than a stand-alone energy system. This approach is possible because the hybrid system can take advantage of some of the benefits and overcome some of the drawbacks of both energy resources. To achieve the above outperformance, it is necessary to have ample solar and geothermal resources in the same places. Is this requirement met all over the nation or the whole world? The following part will include an analysis and a discussion of this topic.

Figure 4a, which originates from the National Renewable Energy Laboratory (NREL) of the Department of Energy (DOE) of the United States, depicts the most prospective regions for CSP facilities located all over the globe. Figure 4a also represents the geothermal resources with the highest recorded temperatures. One can observe that some of the "sweet spot" locations for geothermal and solar energy overlap, which creates the foundation for merging the two kinds of renewable energy (Spadacini et al., 2016). Taking China and the United States as specific examples, Fig. 4b-c illustrates the distribution of solar and geothermal resources in those countries. This figure also demonstrates, to some extent, the distribution consistency of the two renewables in both countries (Wang, 2015).

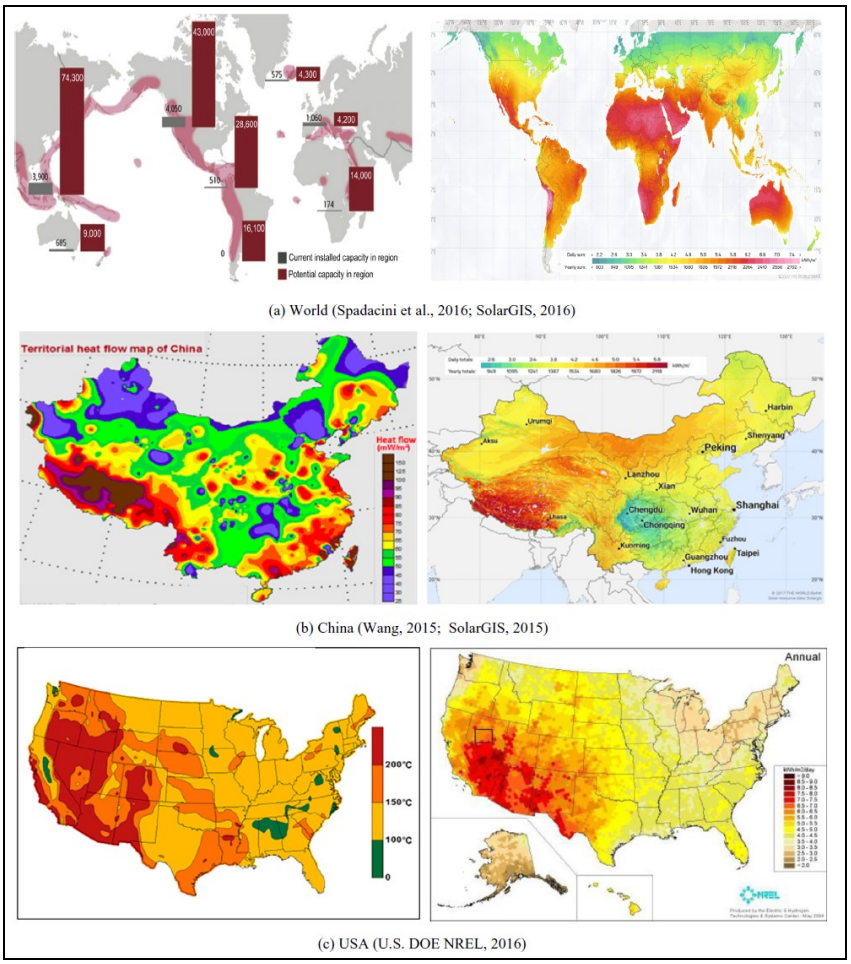

Figure 4. Distribution of geothermal heat flux (left side) and solar radiation index (right side).

2.2.1 Recent Developments in Solar-Geothermal Combined Systems

Finlayson and Kammer published their analysis of a solar-geothermal hybrid system as early as 1975. Their studies brought a great deal of attention to solar-geothermal hybrid systems for the production of electricity (Dimarzio et al., 2015; Ghasemi et al., 2014; Kondili and Kaldellis, 2006; Mathur, 1979). A hybrid system inherits the benefits of using solar and geothermal energy sources because of the reciprocal compensating that occurs in the energy qualities and structures. When the hybrid solar-geothermal power plants were run in an operating mode that was utterly optimized, it was discovered that their thermodynamic performance was superior to that of the stand-alone plants. The higher solar irradiation, higher geothermal fluid temperatures, and lower ambient temperatures all contribute to an increase in the amount of net electricity hybrid power plants produce. In addition, hybrid solar-geothermal power plants have the potential to be cost-competitive. Recent research has shown that solar-geothermal systems have a significant promise for multigenerational applications, including producing energy, heating, cooling, and even freshwater (Calise et al., 2016; Ruzzenenti et al., 2014; Tempesti et al., 2012).

In their study from 2006, Lentz and Almanza looked into whether or not it would be possible to use a parabolic trough solar field to boost the enthalpy of fluids coming from geothermal wells, hence increasing the amount of steam produced. The system's conversion efficiency from heat to electricity may be improved at greater temperatures. On the other hand, avoiding the precipitation of certain salts became feasible because of the rise in steam-water flow rates. This approach was achievable since the solubility of the salts was improved. An integrated technique for constructing a geothermal-solar greenhouse was proposed by Kondili and Kaldellis (2006) to reduce the amount of fossil fuel used.

The technique was put into practice in a particular location, demonstrating that the suggested system configuration was economically desirable.

Boghossian (2011) researched a Kalina geothermal-solar hybrid cycle that used a mixture of ammonia and water as its working fluid. He then compared the performance of this cycle to that of two independent single energy-mode plants. These plants were a geothermal binary organic plant and a solar thermal steam plant. Based on a comparison of design power, it was discovered that geothermal and solar energy modes do not have any synergy. To be more specific, the hybrid plant generates net power that is about 29 percent lower than the combined single-energy mode plants. Because solar cells have a negative temperature-dependent characteristic of 0.4-0.5

percent /°C, Nielsen and Brgesen (2012) optimized a geothermal heat pump supplemented by a hybrid solar system by cooling the solar cells. As a result, the electric efficiency of the system increased by up to about 20 percent. The heat extracted from the solar cells may also be used, resulting in a lower requirement for an external energy source and hot water.

A binary geothermal system that utilizes sun boosting was suggested by Zhou et al. (2013). They looked at the impact that factors such as solar irradiance, ambient temperature, the quality of the geothermal resource, and geographical position had on the overall performance of the hybrid system. When compared to solar and geothermal facilities that operate independently, electricity production has the potential to be significantly boosted. In addition, it was discovered that the hybrid plant's net power production could be increased by either decreasing the ambient temperature or increasing the sun irradiation and the temperature of the geothermal reservoir (Ayub et al., 2015). Ghasemi et al. (2014) developed a model to hybridize the ORC geothermal power system with a low-temperature solar trough facility. The solar trough facility was used with the geothermal system to evaporate a portion of the working fluid. It should come as no surprise that the hybrid system performed better. Compared to stand-alone geothermal and solar systems, the hybrid system's statistics revealed a 5.5 percent increase in yearly power output and a 17.9 percent rise in efficiency, respectively. In addition, the hybrid system showed a greater maximum second law efficiency of about 3.4 percent compared to individual geothermal and solar systems at all ambient temperatures tested.

An integrated model for a hybrid solar-binary geothermal system was created by Ayub et al. (2015). They claimed that the LCOE might be minimized by 2 percent for the hybrid system compared to the stand-alone geothermal system. LCOE decreased by about 8 percent was achieved due to optimizing the stand-alone geothermal ORC. The significant initial investment required by ORC systems is one of the primary challenges that must be addressed and overcome. A decrease in LCOE of 8 percent is significant and valuable for the economics of ORC systems suited for low-enthalpy geothermal resources. A thermodynamic model was proposed by Cardemil et al. (2016) to evaluate the performance of single- and double-flash geothermal power plants that were assisted by parabolic trough solar concentrating collector field. This evaluation took into consideration four different geothermal reservoir conditions. Depending on the features of the geothermal resource, the hybrid single-flash power plant has the potential to provide at least 20 percent more power production than it does now. In addition, the energy efficiency of the process was improved in the examples studied by a minimum of 3%. The developed model also allowed for assessing the reduction in the consumption of the geothermal fluid from the reservoir when the plant power output remains constant. This reduction can be as high as 16 percent for the hybrid single-flash and as high as 19 percent for the hybrid double-flash.

Calise et al. (2016) created an innovative solar-geothermal poly-generation plant that was intended to serve a small community with electrical energy, thermal energy, cooling energy, and freshwater simultaneously. The hybrid system was designed using a photovoltaic thermal collector (PTC) and an Organic Rankine Cycle (ORC) powered by medium-enthalpy geothermal energy. The geothermal brine was also used to heat and cool the inside of buildings. The heat for a multi-effect distillation machine, which produced desalinized water from saltwater, was supplied by geothermal fluid. During the "Thermal Recovery Mode operation," the results revealed that the global exergy efficiency ranged between 40 and 50 percent. However, during the operation known as "Cooling mode," it varied between 16 and 20 percent. In addition, it was discovered that the exergoeconomic costs of electricity, chilled water, cooling water, and desalinated water varied accordingly between the ranges of 0.1475- 0.1722 €/kWh, 0.1863-0.1888 €/kWh, 0.01612-0.01702 €/kWh and 0.5695-0.6023 €/kW hex.

Jiang et al. (2017) constructed the CO_2-based EGS to be included in the solar power plant. Compared to the stand-alone CO_2-EGS and CO_2- solar thermal systems, the hybrid system had an efficiency equivalent to or greater than the total of the two individual systems. In addition, the operating pressure in the hybrid system was lowered, and the recompression compressor was eliminated, which contributed to a drop in the costs associated with the installation and maintenance of the system. In their research published in 2018, McTigue et al. examined four ways of adding solar heat to a double-flash geothermal plant. After the first flash tank, the strategy that involved warming the brine was determined to be the most effective. The amount of solar heat added to this brine had an efficiency of 24.3% when producing electricity. Compared to previous approaches, this one had a lower potential for the minerals to deposit themselves on the heat exchangers. Because the power block, piping, and condenser that are already there might be reused, retrofitting in this manner may be more cost-effective.

2.2.2 Different Types of Solar / Geothermal Hybrid Systems

According to the existing literature and publications, the configurations of hybrid solar-geothermal power generating systems may generally be broken down into the following categories:

1. Solar preheating configuration in which solar energy is employed to preheat the brine either by raising the brine temperature or its dryness proportion (i.e., the steam quality).

2. Solar superheating configuration solar energy is used to superheat the working fluid in a geothermal power cycle in this configuration.

3. A configuration for geothermal preheating, in which geothermal energy is utilized to preheat the feed water in a solar thermal power plant that uses a steam Rankine cycle.

4. Additional up-and-coming ideas

3. CASE STUDY- CLIFTON, ARIZONA

3.1 Geology

3.1.1 Safford basin

Roughly 300 kilometers in length, from Globe, Arizona to well past the Mexican border, is an extensional basin with a northwest-to-north trend; there exists Safford Basin. The Gila, Peloncillo, and Whitlock Mountains form the northeast and east boundaries of the Safford Basin. They are composed primarily of mid-Tertiary volcanic rocks, with some minor Laramide volcanic and some intrusives in the Gila Mountains area. The Tertiary granitic rocks of the Santa Teresa Mountains and the Precambrian granitic rocks of the Pinaleno Mountains form its southwestern boundary (Thorman, 1981). Two major rivers drain the basin, the San Simon River and Stockton Wash, which drain the southeast corner of the basin; both do not flow regularly, while the Gila River, which flows year-round, drains the basin's northwest region.

More than 4,600 meters of playa, fluvial, and lacustrine sediments filled the basin (Kruger, 1991). There are no outcrops of volcanic rocks within the basin besides tephra deposits. Safford Basin formation likely started 17 million years ago, based on the ages of volcanic rocks in the surrounding mountains to the north and east. Basin and range crustal extension may be dated to this period by its overlap with the ages of the youngest intermediate-composition volcanic rocks from the middle Tertiary and the oldest basaltic-composition lava flows (Richter et al., 1983).

3.1.2 Stratigraphy

The sedimentary rocks that comprise the basin infill of the Safford Basin were deposited in two discrete packets, defined by a gap in the deposition in a geologic period as is typical of basins in southeastern Arizona and southwestern New Mexico (Menges and McFadden, 1981). Miocene Midnight Canyon Conglomerate, deposited between 10 (age not certain) and 17 million years ago, is the older lower basin-fill unit. It could be seen in the lower Bonita Creek Basin and the Gila Box outlet, Richter et al., (1983). Houser et al. (1985) also agree with Richter. Pliocene 111 Ranch Formation, Bear Springs deposits (2 to roughly 6 Million years ago), and an unmapped Pliocene or lower Pleistocene unit above it make up the younger upper basin-fill layers. The Safford Basin's upper basin fill is exposed everywhere below the Pleistocene layers.

About 2 million years ago, sedimentation in the basin stopped when the basin's sinking slowed, and through-flowing drainage was formed. The unnamed unit may have documented the beginning of the change from a closed basin to through-flowing drainage. While the older units lack obsidian, which is present in the younger unit, it does have the remainder of the array of characteristic clasts carried by the Gila River. The Eagle Creek and San Francisco River drainage basins, to the north and west of Clifton-Morenci, are likely the origins of the obsidian (Figure 5). An unmapped younger unit containing obsidian is found overlying the Pliocene 111 Ranch Formation in the Safford Basin. The obsidian-bearing unit was delineated as the beds of Smuggler Canyon on the northwest edge of the Duncan Basin (basin towards the east Safford Basin), Ferguson and Enders (2000).

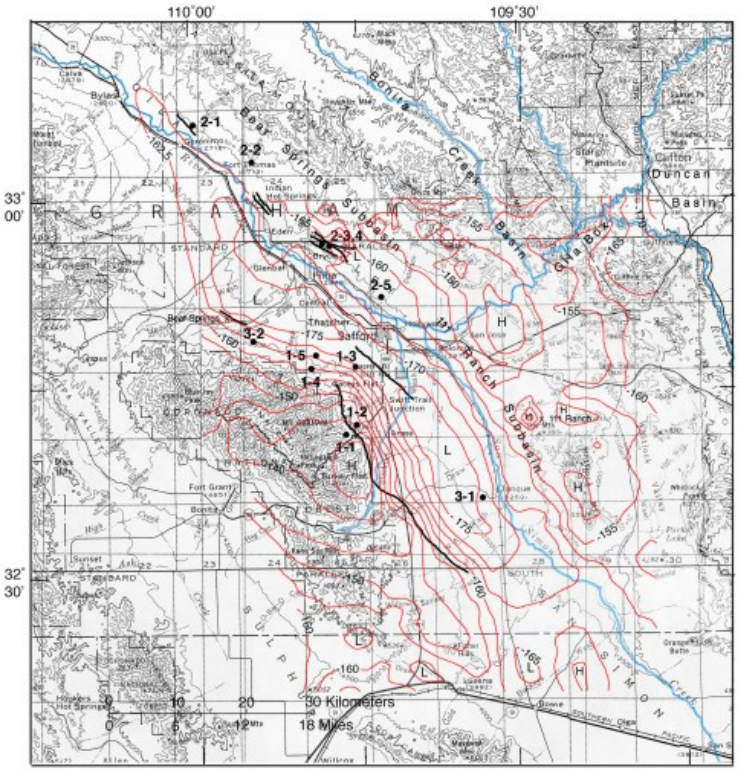

Figure 5: Safford Basin, its subbasins, the surrounding mountain ranges, and the critical waterways that drain into it are depicted in blue lines. Thick black lines represent faults. The red contours of the Bouguer gravity anomaly are displayed(Houser et al., 2004)

Gila River terrace alluvium, which is about 24 m above the elevation of the current river, and piedmont alluvium from the Gila, Peloncillo, and Whitlock Mountains to the north and east, and the Pinaleno and Santa Teresa Mountains to the southwest, make up the Pleistocene units of the Safford Basin. The floodplain of the Gila River and the surrounding washes contain alluvium dating back to the Holocene. In every case, the basin fill units are placed right on top of the alluvium from the Gila River terraces. Piedmont alluvium lies on top of either basin fill or Gila River terrace alluvium, with minimal contact between the two. A band of terraces along the northern bank of the Gila River at its basin entry is roughly five kilometers long. It contains the river's oldest alluvial deposits (Houser et al.,1985). However, since 0.6 million years ago, the river appears to have stayed within the modern Holocene flood plain's lateral boundaries.

3.1.3 Structure

Figure 1 shows the outline of the Safford Basin and its associated subbasins as determined by the imprecise Bouguer gravity anomalous contours (Wynn, 1981). Safford Basin is a semi graben; its deepest part lies in the southwest adjacent to the Pinaleno Mountains, overlain by the Pinaleno Mountain detachment fault (Thorman, 1981), as evidenced by gravity data and Vibroseis seismic reflection data after Kruger, 1991. The basin comprises two subbasins; one lies between Cactus Flat and Tanque in the southern part, while Thatcher and Fort Thomas make up the northern one (Figure 5). Safford is located in the approximate center of the trough that demarcates the two subbasins. Seismic reflection measurements show that the southern subbasin is as deep as 4.6 km, but a drill core obtained from the base of a deep water well south of Thatcher reveals that granite underly the trough at an approximate depth of 0.76 km (Kruger 1991). As a result, there is at least 3.5 km of elevation on the bedrock surface at the basin's base.

Because a Pliocene vertebrate fossil location was discovered around Dry Mountain (Figure 5) in the eastern part of the southern subbasin, it was given the name "111 Ranch subbasin," and the northern subbasin is referred to as the Bylas subbasin.

The correlation between superficial evidence of Quaternary faults and the shapes and sites of the deeper sections of the subbasins is an essential element of the Safford Basin's subsurface shape (Figure 5). At the western margin of the 111 Ranch subbasin, the Safford Fault zone (Figure 6) runs side by side and ends towards the north. As the saddle between the two subbasins rises to a crest, the Cactus Flat Fault follows that rise. It rends in the NWSE direction. Faults can be found along the Bear Springs subbasin's northern margin.

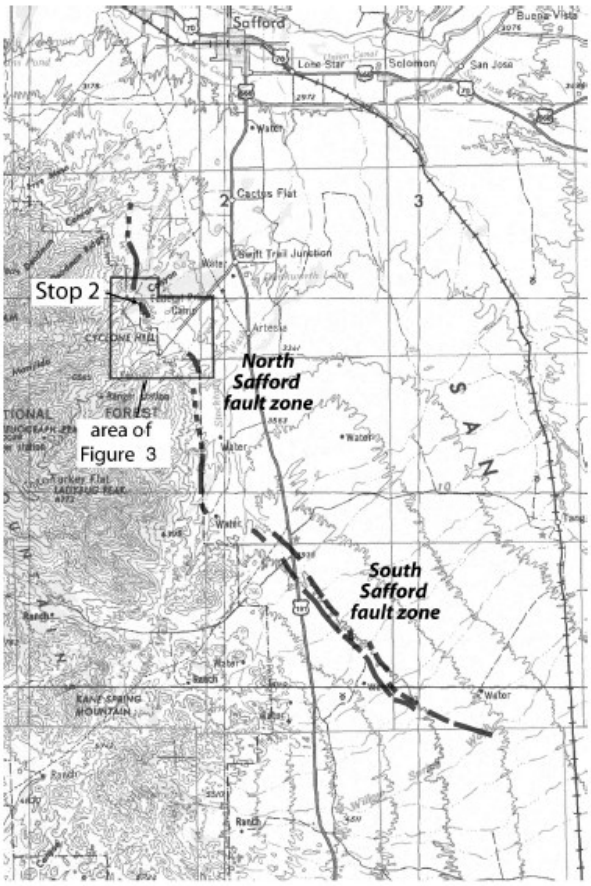

Figure 6: shows the Safford basin fault zone. There are two distinct parts to the fault zone, one in the north and one in the South, each with its orientation and trend concerning the mountain range's front. (Houser et al., 2004)

Continued depression of the underlying Bylas subbasin is reflected in the vast alluvial plains at the lower streams that drain the northeast side of the Pinaleno Mountains. Valleys filled with Holocene alluvium are narrower than 0.4 kilometers in width in places where northeast-flowing streams run over the northeast-slanting slope of the subbasin. Where the streams cross the axis of the underlying subbasin and run above the southwest slanting side of the subbasin, the valley widths suddenly broaden to up to 4 km. This approach implies that the degree of the slope of the northeast-running streams is greater above the northeast-slanting side of the

subbasin and less significant above the southwest slope. Safford Basin is still being sculpted by the same tectonic processes that have been at work for the previous seventeen million years, albeit at a diminished activity rate.

3.1.4. Tectonics

The tectonic activities that led to the evolution of the South Eastern basin of Arizona can be reconstructed using the deformation structures overprint on the mylonitic rocks formed by the detachment faulting often associated with wide-reaching extensional tectonism, lineation, and their trend show direction sense (southwest) of the shearing force and magnitude, age can be inferred by the analysis of radioactivity of some elements in the volcanic rocks and plutonic intrusions. Recreating the path of the detachment fault based on several features shows that displacement is estimated to be between 40 and 60 kilometers, with a more significant displacement in locations toward the South. Granitoid magmatism occurred between 24 and 26 million years ago after widespread volcanism between 26 and 28 million years ago during the early stages of extensional basin formation. According to the results of 40Ar/39Ar dating on mica, the cooling of footwall mylonites did not stop until 22 to 24 million years ago (Spencer et al., 2022).

3.2 Geothermal in Clifton, Arizona

The previous studies provide the following information concerning the potential of geothermal energy in the Clifton study area based on geology, geophysics, geochemistry, and limited test drilling (Brown,2006).

It seems that the geothermal system is all left of what was once a much bigger system than the one we see today. Indications of widespread condensate rock modification in the relatively recent gravel terrace deposits at higher elevations suggest that this more extensive system was used as late as 10,000 years ago. The faulting on both the east and west banks of the San Francisco River seems to be closely linked to the system. The most recent rock modification and the hottest spring orifices seem confined around these junctures due to crossing faults like the Limestone Gulch Fault or other cross-cutting structures. If so, it may be because cross-faulting also concentrates the heat from upwelling in one area. Hot spring water has been analyzed using geothermal methods, and the results suggest the existence of a geothermal reservoir at 130 degrees Celsius or more. Gradient drilling and temperature recording have shown a deep geothermal system with temperatures that may match or even surpass those anticipated by geothermometry. Drilling data further corroborate the close relationship between the faulting discovered via field mapping and the upwelling plumes of thermal water. In the San Francisco Canyon region, there may be a good chance of success if geothermal test wells are strategically placed to intersect deep faults(Brown,2006).

The Diorite Porphyry (Map Unit Tpd) found in the Tertiary era is the topic of this research. Extending from the mouth of Casius Canyon to the north bank of the San Francisco River opposite Oroville, outcrops of this Paleocene (65 to 54.8 Ma) unit may be seen on the west bank of the river, opposite the Potter Ranch. A massive, severely altered sill-like structure has intruded the Longfellow Limestone, forming this outcrop. The unit occurs on the river's east bank as thick dikes that intrude both Pre-Cambrian and Paleozoic era rocks. On the north side of Clifton Peak, a rather large outcrop of undisturbed rock was discovered, and it was either in touch with or surrounded by flows of the Tertiary Andesite unit. In the San Francisco River Canyon, this section represents the Laramide intrusive. All older rocks in the Clifton-Morenci area have been invaded by this unit, which is widespread in the region. It is conceivable that it may be located in the geothermal reservoir. They intrude on the earlier rocks as dikes, sills, laccoliths, and lappoliths. Copper mineralization in the Morenci Mine results from diorite porphyry and related units, which are widespread in the region. In TG-2, this intrusive unit was found above and below the Longfellow Formation. Some potassium feldspars and the euhedral quartz crystals have undergone embayment and resorption, and the matrix has changed from hard rock to soft clay in the drill hole (Brown,2006).

3.3 Solar Energy in Clifton, Arizona

In Clifton, Arizona, the average annual solar radiation value is 6.67-kilowatt hours per square meter per day (kWh/m2/day) (Figure 7). Values from the Clifton scale may be compared to the American range's low and high ones (Solar Energy Local, 2023).

- With its 1% greater average monthly sun radiation, Clifton is an excellent example of a state with relatively high average monthly solar radiation.
- For example, Clifton's monthly average sun radiation is 70% greater than Washington's low monthly average solar radiation.

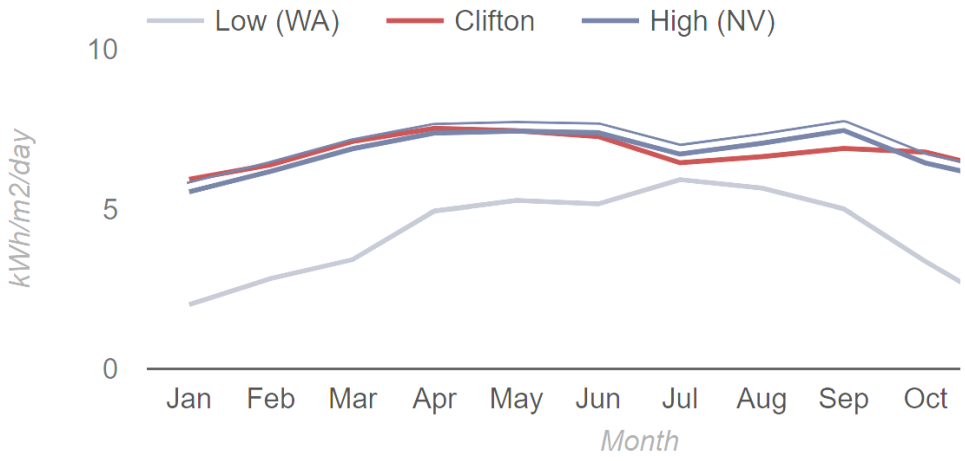

Figure 7. Clifton, Arizona's average monthly solar radiation (Solar Energy Local, 2023)

The latitude of Clifton, Arizona, is 33.02 degrees. Clifton's optimal solar panel tilt is as follows (Solarific,2023):

- The angle of the solar panels is toward the South to maximize their efficiency.
- The most productive angle for putting solar panels in a fixed location, such as a roof, is 28.2 degrees.
- The optimal tilt for photovoltaic panels is 9.7 degrees in the summer and 48.1 degrees in the winter, meaning adjusting twice a year is necessary.
- The most efficient angle for the solar panels varies throughout the year, from 6.1 degrees in the summer to 53.4 degrees in the winter and 30.1 degrees in the fall and spring.

Table 2 shows how Clifton's sun radiation levels stack up against other U.S. locations. We can evaluate Clifton levels by contrasting them with 1) low average solar radiation levels in Washington (W.A.) and 2) high average solar radiation levels (H.A.) in Nevada (N.V.) (Solar Energy Local, 2023).

Table 2.Comparison of Clifton, high, and low solar power

Month	Low	Clifton	High
Dec	1.76 k/m/d	5.45 k/m/d	4.93 k/m/d
Nov	1.87 k/m/d	6.16 k/m/d	5.87 k/m/d
Oct	3.36 k/m/d	6.78 k/m/d	6.44 k/m/d
Sep	5.01 k/m/d	6.9 k/m/d	7.46 k/m/d
Aug	5.66 k/m/d	6.64 k/m/d	7.06 k/m/d
Jul	5.92 k/m/d	6.45 k/m/d	6.72 k/m/d
Jun	5.16 k/m/d	7.27 k/m/d	7.39 k/m/d
May	5.27 k/m/d	7.45 k/m/d	7.44 k/m/d
Apr	4.94 k/m/d	7.53 k/m/d	7.38 k/m/d
Mar	3.42 k/m/d	7.12 k/m/d	6.89 k/m/d
Feb	2.83 k/m/d	6.39 k/m/d	6.18 k/m/d
Jan	2.01 k/m/d	5.93 k/m/d	5.54 k/m/d
→ k/m/d: kilowatt hours per square meter per day.			

4. MODELING APPROACH

4.1. Geothermal Reservoir Modeling

4.1.1 Geothermal Reservoir Modeling Parameters

In order to build a geothermal reservoir model, we need to collect and calculate the reservoir's petrophysical and geomechanical properties data.

Table 3 summarizes the input parameters that we used in our modeling.

Table 3. Input parameters for geothermal reservoir modeling in Clifton, AZ.

Rock Type	Permeability [2]		Porosity[2]		Thermal Conductivity[1]	Volumetric Rock type Thermal expansion (10^{-5} per °C)[3]	Density (kg/m^3)[4]	
Diorite	Fractured : 0.4D		Fractured 2.9		2.5Wm^{-1} K^{-1}	2.1	2800-3000	**Poisson's Ratio[4]**
	Matrix : 0.338 µD		Matrix 0.1-0.5 %					0.1-0.2
	Specific heat (10^3 J/kg K)[3]					**Geothermal Gradient (°C km^{-1})[1]**	**E (Gpa)[4]**	
	Temp. (°C)	0	50-65	200	400			
	0.71	0.81	0.99	1.09	1.18	40	30-100	

References:

1	*Morgan, P. (2016). A simple model of gravitationally-driven water flow in a semicircular aquifer to estimate geothermal power potential: Examples from Arizona and Colorado. Geothermics, 64, 28–41. https://doi.org/10.1016/j.geothermics.2016.04.006*
2	*Wolff, R.G. (1982). Physical properties of rocks; porosity, permeability, distribution coefficients, and dispersivity.*
3	*Goranson, R.W., (1942). Heat capacity of rocks, in Handbook of physical constants, Birch, F., ed: Geological Society of America Special Paper 36, Table 16-2, p. 235-236.*
4	*Typical Properties for Various Rocks. (n.d.). https://structx.com/Soil_Properties_010.html*
5	*Faoro, I., Niemeijer, A., Marone, C., & Elsworth, D. (2009). Influence of shear and deviatoric stress on the evolution of permeability in fractured rock. Journal of Geophysical Research: Solid Earth, 114(B1). https://doi.org/10.1029/2007jb005372*

The mass flow and heat recoverable were evaluated for each combination of parameters modeling the geometry of a vertical section. A thermal simulator was used to develop a mathematical model where Darcy's law equation is applied to design the velocity of a fluid phase; this model describes the interactions between permeability, saturation, viscosity, and pressure difference. The thermal model considers the water phase (w) and steam phase (s) in our case (McClure, 2022)

$$u_w = \frac{\bar{K} k_{rw}}{\mu_w}\left(\frac{\partial P_w}{\partial x_j} - \rho_w \bar{g}\right) \quad (1)$$

$$u_s = \frac{\bar{K} k_{rs}}{\mu_s}\left(\frac{\partial P_s}{\partial x_j} - \rho_s \bar{g}\right) \quad (2)$$

Where u is the velocity of phase, μ is the viscosity of phase, P is the pressure, $\bar{K}$ permeability, and gravitational acceleration. The mass balance of water and steam is defined as:

$$-\frac{\partial(u_w \rho_w)}{\partial x_i} + q_w - d_v = \frac{\partial(\phi S_w \rho_w)}{\partial t} \quad (3)$$

$$-\frac{\partial(u_s\rho_s)}{\partial x_i} + q_s + d_v = \frac{\partial(\phi S_s\rho_s)}{\partial t} \quad (4)$$

Where ρ is the average density, q is the volumetric flow rate, d_v is the vaporization rate, Sw is the water saturation, and Ss is the vapor saturation. Equations are reorganized, and the flow rate is described in the porous medium, considering a pressure difference between the two phases. This pressure difference is defined as capillary pressure $P_c = P_s + P_w$.

$$\frac{\partial\left\{\frac{\bar{K}k_{rw}\rho_w}{\mu_w}\left(\frac{\partial P_w}{\partial x_j} - \rho_w\bar{g}\right)\right\}}{\partial x_i} + q_w - d_v = \frac{\partial(\phi S_w\rho_w)}{\partial t} \quad (5)$$

$$\frac{\partial\left\{\frac{\bar{K}k_{rs}\rho_s}{\mu_s}\left(\frac{\partial P_s}{\partial x_j} - \rho_s\bar{g}\right)\right\}}{\partial x_i} + q_s + d_v = \frac{\partial(\phi S_s\rho_s)}{\partial t} \quad (6)$$

Equation 6 shows the energy balance of water, steam, and rock, assuming that the movement of steam and water through the reservoir is adequately slow, the surface area of water and steam is amply large, the thermal equilibrium exists between water, steam, and rock (Mercer et al., n.d.-a). Hence, considering these assumptions, it is possible to describe the energy-balance equation:

$$-\frac{\partial(u_w\rho_w H_w + u_s\rho_s H_s)}{\partial x_i} + q_w H_w + q_s H_s + \frac{\partial(\bar{\bar{K}}_m\frac{\partial T}{\partial x_j})}{\partial x_i} = \frac{\partial(\phi\rho H + (1-\phi)H_r\rho_r)}{\partial t} - \frac{\partial\phi p}{\partial t} + (u_w + u_s)\frac{\partial p}{\partial x_i} \quad (7)$$

Where H_s is the enthalpy of saturated steam, H_w is the enthalpy of saturated water, T is the reservoir temperature, $\bar{\bar{K}}_m$ is the thermal dispersion tensor for the medium, ρ_r is the average rock density, and h_r is the rock enthalpy. H is the total enthalpy of the mixture, and it is defined as H=(Ss ρsHs+ Ss ρsHs)/ρ.

4.1.2 Flow Rate Modeling

The mass flow rate is evaluated to determine the recoverable energy (McClure, 2022). The recoverable energy (j) in a period is defined as:

$$Q_{rec} = \dot{q}c_w(\Delta T_j)\,(\Delta t_j) \quad (8)$$

Where c_w is the heat capacity of the fluid produced, $\dot{q}$ is the mass flow rate, Δt_j is the period of the project (30 years), and ΔT_j is the difference between production temperature and the power plant outlet temperature (T. Li et al., 2016).
The thermal energy to generate electricity is calculated with the following equation:

$$E_j = Q_{rec}eff \quad (9)$$

Where eff is the net cycle thermal efficiency, this project uses a net cycle thermal efficiency of 10 %.

4.2 Solar Modeling

4.2.1 Collector System

We propose the Concentrated Solar Power (CSP) system for this project. In the early 20th century, Frank Shuman realized that increasing solar thermal energy required concentrating sunlight. It has been suggested that flat plate collectors are the easiest way to concentrate the sun's energy in the form of heat. A darkening panel faces the sun, often near the equator for optimum exposure, and fluid is circulated via tubes underneath to soak up the heat. This liquid (often water) may be used commercially or in the home. The vacuum insulation of evacuated tubes allows them to absorb heat much faster, leading to greater temperatures and efficiency (Tyagi et al., 2012).

In addition, the collectors in this system can be classified into four categories:

- Parabolic trough collectors
- Linear Fresnel reflectors
- Power tower reflector/receivers
- Parabolic dish reflectors

Studies have revealed that the parabolic trough systems shown in the following figure are the most cost-effective and extensively utilized systems for producing power worldwide. (Qazi, 2017) We thus recommend the parabolic cylinder concentrator for usage in Clifton, Arizona (Figure 8). Nearly 90% of the current CSP infrastructure is based on this technology. In this setup, the sun's rays are concentrated on a receiver pipe (absorber tube) at the focal point of parabolic troughs. A long parabolic-shaped collector with curved mirrors forms. The metal absorber tube is often encased in an evacuated glass tube that runs the trough length (which may be over 600 meters). The troughs are turned as the sun travels across the sky from east to west to get the most out of the sun's rays. Synthetic oil, which can be heated to temperatures up to 400 degrees Celsius, fills the metal absorber tube. Due to the parabolic form, the sun's rays might be magnified by a factor of 30–100 inside the troughs. Next, the fluid is pushed via a heat exchanger, transferring its heat to water, which boils and releases steam. Steam powers a turbine that spins a generator to produce energy. In order to maximize the effectiveness of the plant, it may operate at temperatures as high as 550 degrees Celsius when alternative heat transfer fluids such as molten salts or direct steam are used. Fossil fuels may back up solar thermal power at night or on overcast days in hybrid versions of these systems. (Qazi, 2017)

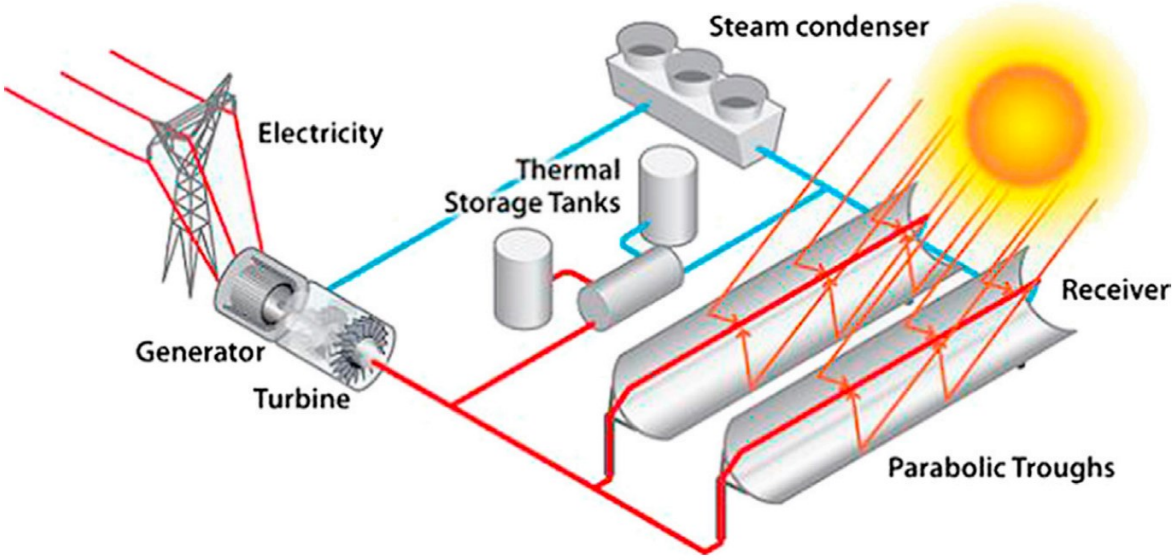

Figure 8. The cylindrical parabolic concentrator system (Qazi, 2017)

In order to find out the exit temperature Tf_o from the CSP, which is an essential factor in deciding the efficiency of the Enhanced Geothermal System (EGS), the temperature output of the solar collector should have the capacity to maintain the minimum temperature difference between the evaporator and condenser by 85 degrees Celsius. Initially, certain assumptions are made before calculating the Tf_o of the CSP.

4.2.2 Solar Modeling Assumptions

Tfi = 160c (Inlet temperature)

Cp= 1.2kj/kgk (Specific heat of water)

M = 50kg/s (Mass flow rate)

Location (Latitude, Longitude)= 34.089n, 111.0937 w (Arizona)

Time = 1400 hours

Concentration width (W)= 2m

N =33rd day

Length = 6 m

Absorber outside diameter 8.8 cm

Absorber inside diameter = 7.5 cm

Overall loss coefficient (Ul) = 6.2 w/m2k

Convective Heat transfer coefficient of absorber (hf) = 205w/m2k

Intercept factor = 0.94

Reflectivity (Ƥ)= 0.86

Collector heat removal factor (Fr) = 0.094

(τα)b = Absorber cover assembly = 0.81

Tamb = 23 c (Arizona)

GHI = 2059.7 KW/m2 (Arizona)

DIF = 45.9 KW/m2 (Arizona)

4.3 Hybrid Geothermal/Solar Modeling

4.3.1 Design of the Hybrid System

Thermodynamic features of the ORC working fluid in various states are needed to develop the hybrid model. The energy equation, specifically the Engineering Equation Solver program (EES), is the most powerful tool for describing and calculating the thermodynamic parameters of an ORC working fluid. Because of this, the academic version of EES will be used to calculate all the thermodynamic parameters of the ORC working fluids. Similarly, the information from the prior section was used for the solar resource evaluation. The heat source temperature needed to power the ORC system may be determined using global horizontal irradiance (GHI) and direct normal irradiance (DNI). A steady-state thermodynamic analysis must also be performed for each thermal conversion unit and ORC unit. For modeling purposes, we use the following assumptions: (1) The computation assumes a steady state (2) heat exchanger pressure decreases are disregarded. (3) component-level heat losses are treated as immaterial. The schematic of the proposed model is shown in figure 9.

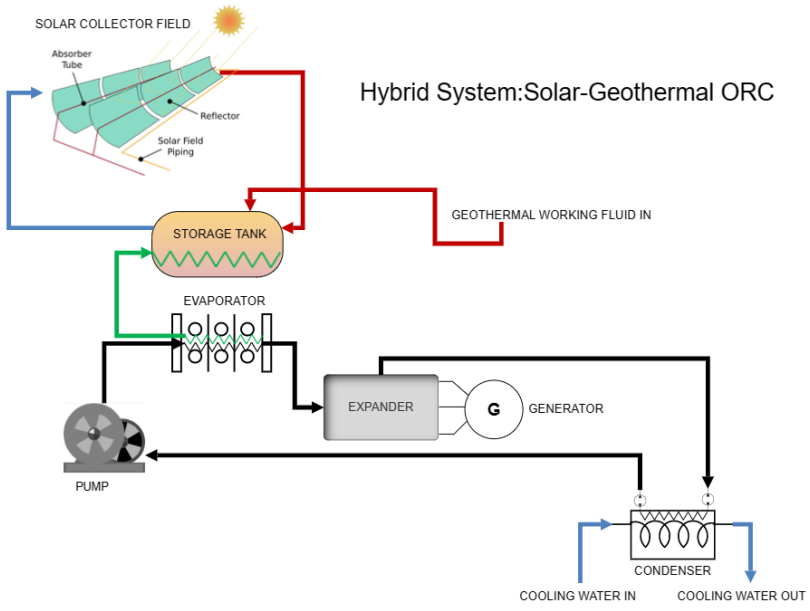

Figure 9. Schematic for the proposed hybrid solar and geothermal ORC System

4.3.2 Model For ORC Subsystems

Each part of the system may use the following generic formulation for the steady-state energy balance:

$$\sum \dot{m}_{in} = \sum \dot{m}_{out} \tag{10}$$

$$\dot{Q} - \dot{W} = \sum \dot{m}_{in} h_{in} - \sum \dot{m}_{out} h_{out} = 0 \tag{11}$$

The subscripts of *in* is the inlet, and *out* is the outlet in the above equations. In addition, $\dot{m}$ is the mass flow rate, h is the specific enthalpy of the streams of the system working fluid, $\dot{Q}$ and $\dot{W}$ are heat transfer and work transfer across the component boundaries, respectively. This system's ORC parts include a pump, expander, evaporator, and condenser.

Following is a description of the primary governing equations used in the creation of the models:

$$For\ Pump: W_p = \frac{\overline{v_p}(P_0 - P_i) \times \dot{m}_f}{\eta_p} \tag{12}$$

where P_o is the pressure at the pump's discharge and P_i is the pressure at the pump's inlet. Moreover, $\dot{m}_f$ is the mass flow rate of the working fluid, η_p is the pump efficiency and v_f is fluid-specific volume.

$$For\ Evaporator: Q_{eva} = \dot{m}_f (h_i - h_0) \tag{13}$$

The Nusselt number, Nu, is defined as the product of the coefficient of the convection heat transfer (h) and the hydraulic diameter of the heat exchanger (D_h), divided by the thermal conductivity (K), whereas the Reynolds number (Re) is defined as the product of the velocity (v), density (ρ), and viscosity of the fluid passing through the heat exchanger (μ).

$$For\ Expander: W_{exp} = \dot{m}_f (h_i - h_0) \tag{14}$$

where inlet and outlet enthalpy at a particular pressure and temperature within and outside the expander are represented by h_i and h_o respectively.

$$For\ Condenser: Q_{con} = \dot{m}_f (h_i - h_0) \tag{15}$$

where inlet and outlet enthalpy at a particular pressure and temperature within and outside the condenser are represented by h_i and h_o respectively.

The laws of thermodynamics stated by the authors form the basis for the aforementioned governing equations (Cengel & Boles, 2014).

4.3.2 Model for Solar Collector

All three types of solar irradiance (beam, diffuse, and reflected) are accounted for in this analysis. The model involves calculating the clear sky global irradiation on a horizontal surface and the clear sky index, diffuse, and beam components on slanted surfaces. The distinct collector type that may be modeled for use is the concentrating collector. Non-tracking and tracking case global and direct beam irradiance data will be collected using parabolic trough technology collectors to inform the development of the model.

For a solar collector, the controlling equation is:

$$\eta = C_0 - C_1 \left(\frac{T_c - T_a}{I_{sol}}\right) - C_2 \left(\frac{(T_c - T_a)^2}{I_{sol}}\right) \tag{16}$$

In this equation, T_c and T_a denote the average temperature of the collector and ambient temperature, respectively; C_o, C_1, and C_2 are collector constants.

Using the collector energy balance equation, we can determine the collector's surface area as follows:

$$\dot{m}_c (h_i - h_0) = G_b \cdot \eta_c \cdot A_c \tag{17}$$

where η_c, A_c, and G_b represent the collector's efficiency, the collector's area, and the surface's global radiation, respectively.

The following equation describes the system's net solar ORC efficiency:

$$\eta_{SORC} = \eta_c \cdot \eta_{ORC} \tag{18}$$

4.3.3 The Hybrid ORC System Analysis: Techno-Economic

The net present value (NPV), payback time, internal rate of return (IRR), benefit-cost ratio (B.C. ratio), and the levelized cost of power generation (LCOE) were all calculated as part of the economic study for the hybrid system. The equations used for the techno-economic analysis of the hybrid system were derived from Baral et al., 2015.

5. RESULTS AND DISCUSSION

5.1. Geothermal Reservoir Modeling

5.1.1 CMG Simulations Results for the Geothermal Model

The Clifton hot spring was the location for this study; however, there are several such spots throughout Arizona. Neither the site nor the surrounding area had been tainted in any way, making it ideal for proposing the installation of the geothermal plants. Although the heat source location was unaffected by the San Francisco River in February and March, it was impacted during the rainy season in July. The hot spring in this area is used for recreational purposed. The pond served as a source for the hot spring, pumped for storage and leisure uses like taking a refreshing dip. This model examines the viability of generating electricity from a geothermal source (hot spring) using an ORC system.

Figure 10 shows the behavior of the downhole and surface temperature of the production well and injection well for 30 years.

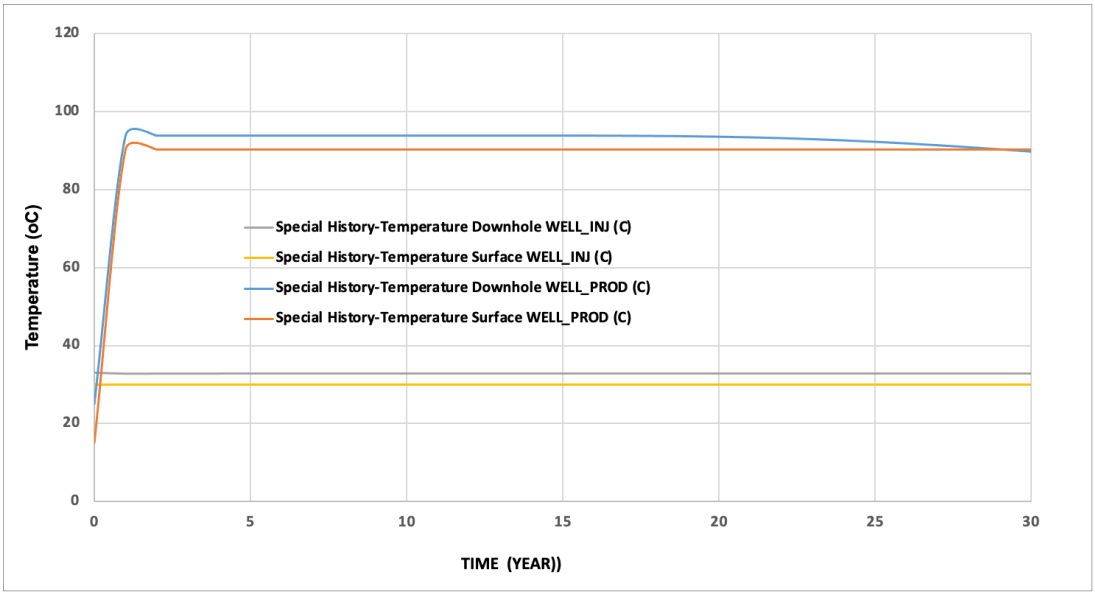

Figure 10.Downhole and surface temperature of the production well and injection well.

In addition, we can observe the changes in the behavior of the flow rate of the production well and injection well over the same period. (Figure 11)

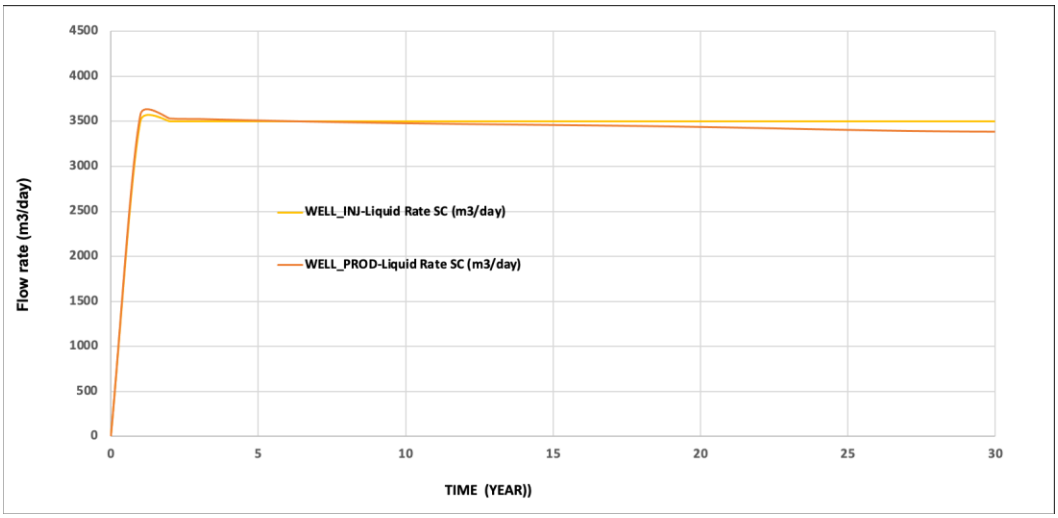

Figure 11.The flow rate of the production well and injection well.

The results of the energy accumulation of the production well can be seen in figure 12.

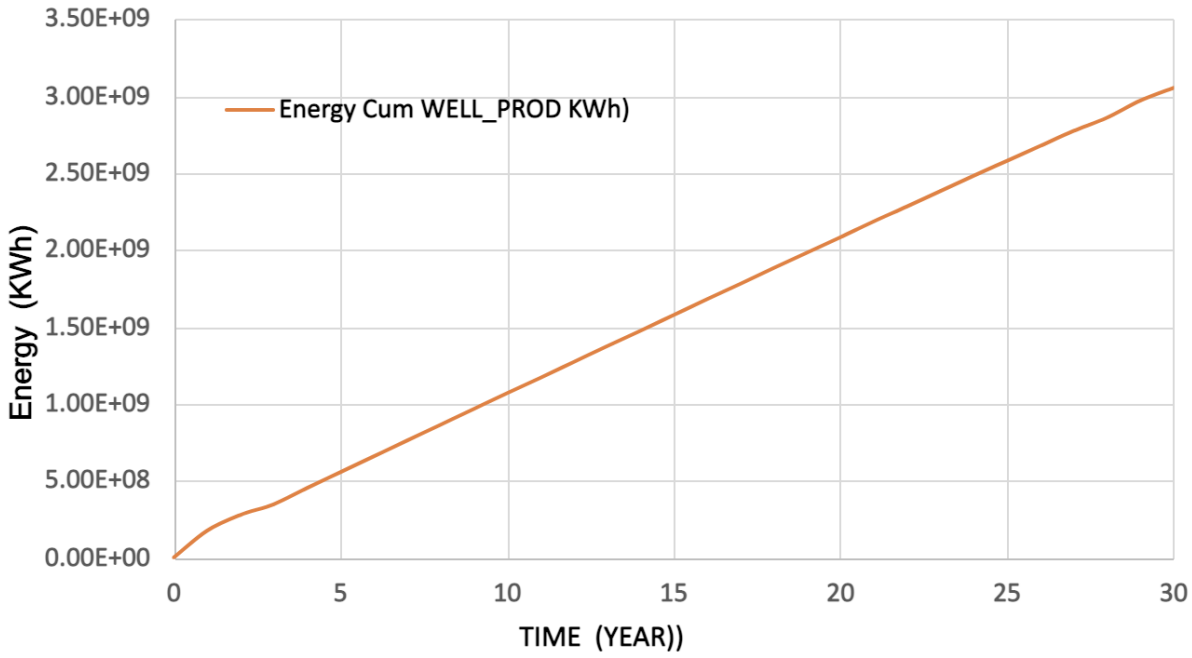

Figure 12.Energy accumulation of the production well.

Table 4 summarizes the output of the simulation for the power generated at the Power plant, which is about 1.16 MW, considering a factor plant of 0.1. The value of power generation is consistent with the previous studies. (Arizona Public Service (APS), 2009)

Table 4. Power generation of the geothermal plant in Clifton, AZ, for 30 years

years	Energy Kwh	Kwh/year	K.W.	K.W.	M.W.	M.W.
30	3.06E+09	1.02E+08	1.16E+04	1.16E+03	1.16E+01	1.16

Moreover, the temperature changes during 30 years can be observed in Figures 13 and 14.

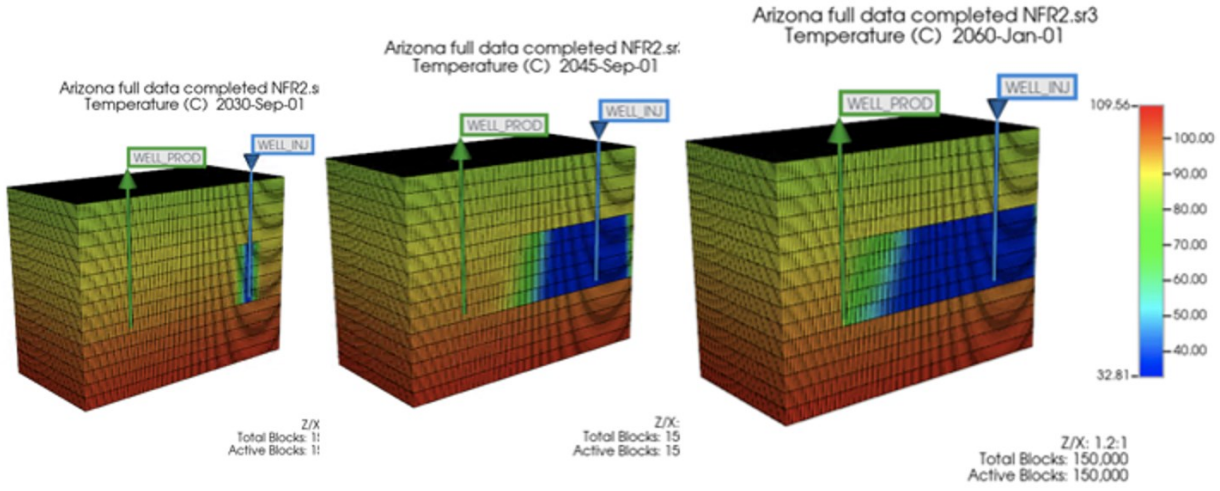

Figure 13. The temperature behavior of the CMG Model of the proposed geothermal injector and producer wells over 30 years

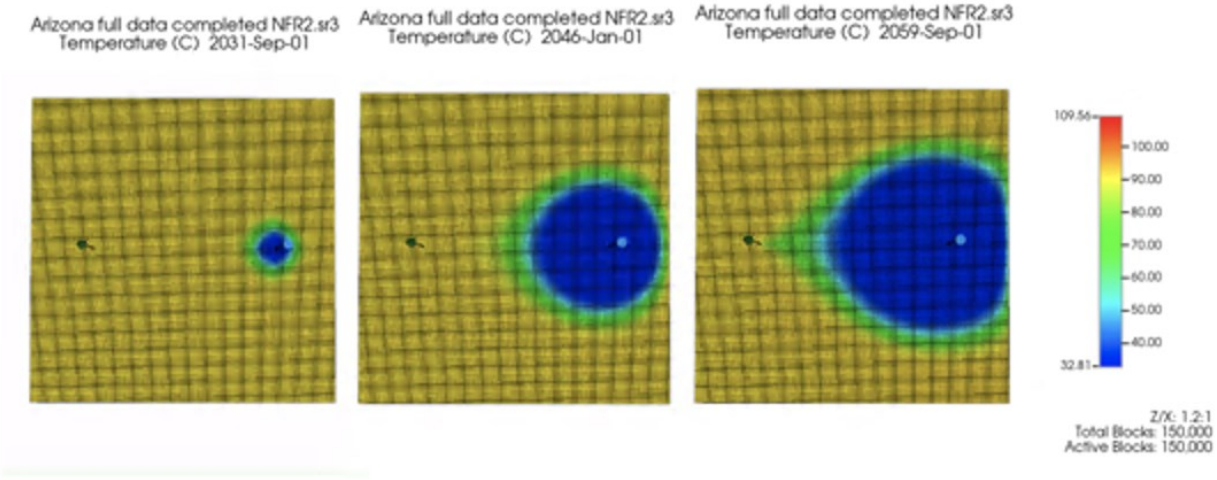

Figure 14. The temperature behavior on the closer view of the CMG Model of the proposed geothermal injector well over 30 years

Based on the data provided above, it may be hypothesized that the Clifton Hot Springs is part of a fracture-dominated groundwater circulation system driven by the piezometric gradient associated with the elevation difference between the Colorado Plateau and the southern Basin and Range provinces. Therefore, the semicircular aquifer model may be successfully applied to the data from this system. This information suggests that the highest aquifer temperature (T_m) is about 180 °C, whereas the springs' outflow temperature (T_0) is 70 °C.

From the Western Regional Climate Center, Desert Research Institute, we obtain a mean annual surface temperature (T_s) of 19 °C; using this value, we can determine that the ratio of the exit temperature, θ_e, to the maximum aquifer temperature, θ_{max}, is 0.32. With this ratio, we get a dimensionless flow rate (ψ) of 1.5; with this rate, we get a dimensionless maximum aquifer temperature of 0.99. Using this data, together with the measured maximum aquifer temperature and the average yearly surface temperature, we could use the equations provided in the following equation to determine the undisturbed maximum aquifer wall rock temperature, T_R.

$$T_R = (\frac{T_m - T_s}{\theta_{max}}) + T_s \quad (19)$$

A temperature of 180 °C was obtained for the unaltered rock temperature of the wall. In order to determine the regional geothermal gradient, we used the previously mentioned value of 100 mWm^{-2} for heat flow and assumed a thermal conductivity for crystalline basement rocks of $2.5Wm^{-1}K^{-1}$. This value yielded a value of 40 °C km^{-1} for the regional geothermal gradient. Since most of the land around Clifton is at a higher elevation and experiences cooler average temperatures throughout the year, we can assume a surface temperature of 19 °C and calculate that the depth range where the temperature is 180 °C, i.e., the maximum depth of the aquifer circulation, *R*, is roughly 4.1 km. Using this value for *R* and the previously estimated dimensionless flow rate of 1.5 and assuming a thermal diffusivity (κ) of 1 $mm^2s^{-1,}$ the aquifer discharge rate of 19 *l/s* (liters per second) was derived.

Witcher (1981) calculated a mean flow of thermal waters from the springs of around 76 l/s based on the difference in the dissolved chloride content of the San Francisco River above and below the hot springs. The semicircular aquifer model estimates a discharge four times less than this amount, but the fact that the two values are so close in size is a good confirmation of the model's utility.

The semicircular aquifer flow model and the dissolved chloride estimate of flow are at odds with one another by a factor of four. One possible explanation for this discrepancy is that the semicircular aquifer model represents a highly simplified geological groundwater flow system that is likely more efficient in heating water with deep penetration over a short distance of horizontal travel in two dimensions. The same outflow temperatures may be achieved with higher flow rates if fracture flow systems were more geologically realistic, horizontal travel lengths were more significant, and major three-dimensional components of the heating were included.

For the second reason, the semicircular aquifer model's assumption of a single aquifer flow may cause it to underestimate flow in the Clifton geotherm system. A variety of temperatures, from 30 to 70 °C, is discharged into the river by the hot springs (Witcher, 1981), which may indicate the merging of two or more thermal aquifer systems or just the mixing of hot and cold water. There are likely other thermal aquifer systems in the area since there are additional thermal springs within a 40-kilometer radius of Clifton. Only the spring with the greatest measured temperature has its flow assessed. The overall flow would be more in line with the estimate from the dissolved chloride technique if it included flows from lower-temperature springs.

5.1.2 Potential Effects on Clifton Geothermal System Development

Providing that all Clifton hot springs discharge at the maximum spring temperature of 70 °C, the maximum thermal energy can be harvested from these waters using the flow rate from the semicircular aquifer model as 4 M.W. thermal, assuming that the waters are cooled to 20 °C. Maximum thermal energy increases to 16 M.W. thermal when the higher flow rate estimate is used from the change in chloride content of the San Francisco River, albeit the total is likely less since not all the hot springs are as hot as 70 °C. Up to several M.W. of thermal energy are accessible at low temperatures, 20-70 °C, depending on the estimations of the maximum thermal energy output of the system from either the semi-circular aquifer model or based on the chloride content estimate of discharge rate. Depending on the flow rate estimate from the semicircular aquifer model and the chloride concentration estimate of the discharge rate, the maximum power that can be extracted from the system is estimated to range from 13 M.W. thermal to 51 M.W. thermal if the system is tapped at its maximum temperature indicated by groundwater geochemistry of 180 °C. Geothermal fluid may create electricity if brought to the surface at temperatures near its maximum. However, only a portion of the maximum thermal power extraction rate from the hot springs is usable. Only as the geothermal fluid cools from its entry temperature into the turbine to its exit temperature into the condenser is energy collected from it. Power extraction from the highest temperature geothermal fluid is estimated to be between 11 and 44 M.W. thermal at a condenser temperature of 40 °C. An efficiency of 6% for a binary power plant (Moon and Zarrouk, 2012) would put the output of this system anywhere between 0.8 and 3 M.W.

5.2 The CSP Analysis Results in Clifton, AZ

5.2.1. The CSP Parameters

Evaluation of Absorbed Heat Flux:

$S = I_bRbP\gamma(\tau\alpha)b + IbRbP\gamma(\tau\alpha)b\left(\frac{Do}{W-DO}\right)$ (Rai 2023)

Ib = GHI – DIF = 1599.8KW/m2

Corresponding to the Given Location and Time:

Latitude = 21.1 N

Declination(33^{rd}) day δ = -9.379

W(14 HOURS LATITUDE) = -20

To Calculate Aperture Tilt (β):

Tan(δ -β) = tan δ/Tanώ

β = 20.774 degree

For Tracking Angle:

CosΦ = Sin^ δ+cos^2 δ*cosώ

CosΦ = 0.89

CosΦz = sinLsin δ+cosL *cosδ *cosώ

cosΦz= 0.78

Rb = CosΦ/ cosΦz

Rb = 1.141

S = 1599*1.41* 0.86*0.81+1599.8*1.141*0.81*(8.8/-20*8.8)
S= 1492.013 W/m2

Concentration ratio = W-Do/3.14*D0 = 7.5

Outlet Temperature of the Fluid :

Tfo = Tfi+ $\frac{Fr*(W-Do)l[s-\frac{u}{c(Tf-Ta)}]}{M*cp}$ (Rai 2023).

Tfo (Outlet temperature) = 185° c

As the results from the CSP model suggest, the inlet temperature is 150° C, and the outlet temperature is 180 °c.

5.3 The Hybrid Solar-Geothermal ORC Model

5.3.1 The Electricity Generation of the Hybrid System

When the temperature of geothermal water decreases in a geothermal plant, the facility's electricity output also decreases; a cylindrical parabolic collector field may compensate for this loss. By increasing the mass flow rates and pressures at the turbine's input, the sun will allow the turbine to operate more closely to the parameters specified in the design. The plant's overall effectiveness and power production will increase as a result. When the geothermal/solar hybrid plant produces less electricity than expected, thermal storage may be used to augment the power output with extra thermal energy. In order to utilize the electricity generated by the hybrid plant when needed, thermal storage is implemented (Michaelides, 2018). As can be seen in Table 5, the system has generated valuable amounts of electricity.

Table 5.Relationship between solar aperture area and hybrid plant thermal efficiency.

Hybrid Power Plant	Solar Aperture Areas (m^2)	Solar Exergy Fraction (%)	Annual Net Power Production (MWh)			Annualized Figure of Merit
			Stand-Alone Solar Plant	Stand-Alone Geothermal Plant	Hybrid Plant	
Subcritical plant	4000	49.07	800	67,290	68,340	0.93
	8000	65.83	1681	67,290	69,291	0.93
	12,000	74.29	2436	67,290	70,076	0.95
	16,000	79.4	3367	67,290	71,107	1.06
	20,000	82.81	3926	67,290	71,716	1.09
	24,000	85.25	4688	67,290	72,478	1.17

During March and April, May, June, August, and September (monsoon and fall, respectively), the hybrid configuration system is considered to be set up. The temperature vs. power relationship shows a steady 30 M.W. of electricity production. The system transitions to a hybrid configuration during daylight hours. The system operates as a stand-alone geothermal power plant after the sun goes down. The hybrid cycle's power production shows a sustained plateau state. Time spent at the plateau is often throughout the day.

5.3.2 The Techno-Economic Evaluation of Solar-Geothermal ORC Hybrid System

This techno-economic research aimed to provide a ballpark figure for the levelized cost of power production using this method. In addition, the monetary indices such as NPV, P.B., and IRR were calculated to determine the particulars of economic significance for producers, financiers, stakeholders, and energy planners. In research from Lemmens (2016), we can estimate the particular cost per kW

of the hybrid solar-geothermal ORC system. The upfront and ongoing expenses of installing an ORC system, whether solar or geothermal, were factored in. Lemmens (2016) was used to evaluate the price of working fluids R245fa and R134a.

Here, the projected system cost for the 30 M.W. power outage plant was $30,750. The solar ORC unit is responsible for the largest possible system share. This component is more costly than solar P.V. because of the high price of the solar collector. The geothermal ORC unit accounts for over 25% of the total project cost, making it the second most expensive component. Production and upkeep costs were included in the economic index's assessment. The hybrid system is expected to be fully installed in one year. The research used a 9% inflation rate (interest rate) and a 30-year lifespan for the system. After 30 years, it is thought that the system has no salvage value at all.

The economic indicators were given based on these assumptions. The output power of a hybrid system using R134a as the working fluid is 25 M.W. (heat source temperature about 80°C). Similarly, while using R245fa as the working fluid at a source temperature of 100 °C, the output power ranged from 30 M.W.

For R134a and R245fa, the hybrid system generates 23 and 32 megawatt-hours (MWh) of electricity annually, respectively. Using a hybrid system, the price of power generation is $0.17/kWh (R134a) and $0.14/kWh (R245fa). The cost of operating two separate hybrid ORC plant systems, which use different working fluids, varies. The cost of R245fa is relatively high compared to other working fluids. Another economic metric is the amount of time it takes for a system to recoup its initial investment. The time it takes for an investment to generate a profit is called the payback period. When the levelized cost of electricity (LCOE) is above $0.38/kWh, the R134a system may achieve a positive return on investment. After eight years of electricity output, the initial investment will provide a profit. The results show that the hybrid solar-geothermal ORC system may be cost-effective when the LCOE is multiplied by the price of electricity generation. When using R245fa as the working fluid, a similar trend is seen. With an LCOE of $0.32/kWh, this investment would provide a return in under ten years. Payback time is seven years when LCOE is $0.34/kWh. Compared to systems that use other working fluids, the system using R245fa has a shorter payback time since it generates more power from the same amount of heat. When the LCOE is 0.36 ± 0.011 $/kWh, the benefit-cost ratio for R134a is 1.5, and the IRR is 9%, whereas those for R245fa are 1.9 and 16%. There are more benefits than costs, making this a doable venture. More importantly, the internal rate of return (IRR) is more than 7%, making this a viable investment option.

6. CONCLUSION

Compared to a fully optimized ORC unit, a geothermal-solar power plant that uses low-temperature geothermal working fluid may produce two to nine times as much electricity with a round-trip efficiency of 83.1%. The geothermal-solar unit has the added benefit of providing consistent (non-variable) electricity throughout its operational hours. The storage capacity is 32 MWh, and the power range is 24.2 MW.

In hybrid units, the working fluid may be heated using solar energy, which also allows for an ORC system. The surplus power may be utilized at peak demand times to offset the increased energy consumption brought on by air conditioning.

This advantageous feature would increase the storage time to 6-10 hours. Because of the inclusion of high-exergy irradiance, the exergetic efficiency of a cycle combined with solar's superheat is lower than that of other kinds of geothermal power plants. However, the thermal efficiency is substantially more significant at 15%. Given the dispersed nature of solar irradiation, substantial collector area and heat storage are required for its collection and usage as part of the heating contribution. Especially in areas where thermal-solar power plants are planned and low-temperature geothermal resources are available, this form of renewable energy power plant will be highly competitive, especially considering the low LCOE of only 0.36 ± 0.011 $/kWh.

7. RECOMMENDATIONS

There are some limitations associated with this study, and we are working on them for further studies.

- While location and most economic data could be paralleled between case study and simulation, many defaults and estimations were used for CSP Watts in cost analysis.
- Limited data from an existing project at Clifton, AZ, led to other assumptions for hybrid system modeling.
- Statistics regarding the exact form of production (PV / CSP) and storage (sensible thermal/geothermal / battery) are not always specified in the case study.
- The study of supercritical CO_2 is suggested in this hybrid system. The CO_2 system has mass flow rates that are up to 3.5 times higher than those for water. Some estimates put the potential efficiency of energy generation from CO_2-based geothermal systems at 1.5 times that of traditional water-based systems. Steam-based geothermal systems might benefit from sCO2 because of their ability to be transported and dissolved in water, which would lessen the risk of pollution, scaling, and deterioration of the power equipment.
- The sensitivity analysis can be carried out to assess the risks associated with investing and funding this project.

- According to the limitations and assumptions associated with the model, using the SAM (System Advisory Model) inputs based on financial parameters, costs, and other economic data, best-fit equipment, loading, and other parameters are recommended.

- Development and testing of heat transfer fluids and site configurations (injector, condenser, expander, evaporator) are warranted. Based on these and other factors, optimal sizing of the solar/geothermal hybrid plant may be better discerned.

REFERENCES

Abdelhamid, M., Pilla, S., Singh, R., Haque, I., & Filipi, Z. (2016, April 12). A comprehensive optimized model for on-board solar photovoltaic system for plug-in electric vehicles: energy and economic impacts. International Journal of Energy Research, 40(11), 1489–1508. https://doi.org/10.1002/er.3534.

Annual Energy Outlook - U.S. Energy Information Administration (EIA). (2022). https://www.eia.gov/outlooks/aeo/

Arizona (U.S. National Park Service). https://www.nps.gov/state/az/index.htm. Retrieved August 2, 2022

Arizona Corporation Commission. (2022). Renewable Energy Standard and Tariff, accessed May 10, 2022.

Arizona Public Service (APS). (2009). ARIZONA'S ENERGY FUTURE: 2009 Renewable Energy Standard Compliance Report. Retrieved October 5, 2022, from https://azcc.gov/Divisions/Utilities/Electric/REST%20PLANS/APS_Compliance_Report_Brochure.pdf

Arizona Profile. (2022). https://www.eia.gov/state/print.php?sid=AZ

Atashnezhad, A., Akhtarmanesh, S., Hareland, G., & Dushaishi, A. M. (2021, June 18). Developing a Drilling Optimization System for Improved Overall Rate of Penetration in Geothermal Wells. OnePetro. https://onepetro.org/ARMAUSRMS/proceedings-abstract/ARMA21/All-ARMA21/ARMA-2021-1215/470287

Ayub, M., Mitsos, A., Ghasemi, H. (2015). Thermo-economic analysis of a hybrid solar- binary geothermal powerplants. Energy 87, 326e335. https://doi.org/10.1016/ j.energy.2015.04.106.

Baral, S., Kim, D., Yun, E., & Kim, K. (2015). Experimental and Thermoeconomic Analysis of Small-Scale Solar Organic Rankine Cycle (SORC) System. Entropy, 17(4), 2039–2061. https://doi.org/10.3390/e17042039

Boghossian, J.G.(2011). Dual-Temperature Kalina Cycle for Geothermal-Solar Hybrid Power Systems.

Brown, D. E. (June 15 ,2006) .GRED III Final Report Clifton Hot Springs Geothermal Greenlee County, AZ, report; Phoenix, Arizona. (https://digital.library.unt.edu/ark:/67531/metadc882124/m1/91/: accessed January 1, 2023), University of North Texas Libraries, UNT Digital Library, https://digital.library.unt.edu; crediting UNT Libraries Government Documents Department.

Calise, F., D'Accadia, M.D., MacAluso, A., Piacentino, A., Vanoli, L.(2016). Exergetic and exergoeconomic analysis of a novel hybrid solar-geothermal polygeneration system producing energy and water. Energy Convers. Manag. 115, 200e220. https://doi.org/10.1016/j.enconman.2016.02.029.

Cardemil, J.M., Cortés, F., Díaz, A., Escobar, R. (2016). Thermodynamic evaluation of solar-geothermal hybrid power plants in northern Chile. Energy Convers. Manag. 123, 348e361. https://doi.org/10.1016/j.enconman.2016.06.032.

Cengel, Y., & Boles, M. (2014). Thermodynamics: An Engineering Approach (8th ed.). McGraw-Hill Education.

Climate Watch. (2022, May 20). The Paris Climate Agreement. Retrieved November 8, 2022, from Climate Watch: https://www.climatewatchdata.org/

Dimarzio, G., Angelini, L., Price, W., Chin, C., Harris, S. (2015). The stillwater triple hybrid power plant: integrating geothermal, solar photovoltaic and solar thermal power generation. Proc. World Geotherm. Congr. 19e25.

Ferguson, C.A. and Enders, M.S. (2000). compilers, Digital geologic map and cross sections of the Clifton-Morenci area, Greenlee County, Arizona: Arizona Geological Survey Digital Geologic Map 1, scale 1:93,750

Fleischmann, D. J. (2006). Geothermal resource development needs in Arizona. Geothermal Energy Association.

Frisvold, G. (2009, January 9). Arizona Solar Energy and Economics Outlook. Arizona Solar Energy and Economics Outlook. https://www.solarthermalworld.org/sites/default/files/story/2015-03-14/arizona_solar_energy_and_economic_outlook_a6875.pdf

Ghasemi, H., Sheu, E., Tizzanini, A., Paci, M., Mitsos, A. (2014). Hybrid solar- geothermal power generation: optimal retrofitting. Appl. Energy 131, 158e170. https://doi.org/10.1016/j.apenergy.2014.06.010.

Houser, B. B., Pearthree, P. A., Homburg, J. A., & Thrasher, L. C. (2004). Quaternary stratigraphy and tectonics, and late prehistoric agriculture of the Safford Basin (Gila and San Simon river valleys), Graham County, Arizona. Open-File Report. https://doi.org/10.3133/ofr20041062

Houser, B.B., Richter, D.H., and Shafiqullah, M. (1985). Geologic map of the Safford quadrangle, Graham County, Arizona: U.S. Geological Survey Miscellaneous Investigation Map I1617, Scale 1:48,000.

Jiang, P.X., Zhang, F.Z., Xu, R.N. (2017). Thermodynamic analysis of a solar-enhanced geothermal hybrid power plant using CO2 as working fluid. Appl. Therm. Eng. 116, 463e472. https://doi.org/10.1016/j.applthermaleng.2016.12.086.

Kondili, E., Kaldellis, J.K. (2006). Optimal design of geothermal-solar greenhouses for the minimisation of fossil fuel consumption. Appl. Therm. Eng. 26, 905e915. https://doi.org/10.1016/j.applthermaleng.2005.09.015.

Kruger, J.M. (1991). Seismic crustal structure beneath the Safford basin and Pinaleno Mountains: Implications for Cenozoic extension and metamorphic core complex uplift in S.E. Arizona: University of Arizona, Dept. of Geosciences, Ph.D. dissertation, 158 p.

Lemmens, S. (2016). Cost Engineering Techniques and Their Applicability for Cost Estimation of Organic Rankine Cycle Systems. Energies, 9(7), 485. https://doi.org/10.3390/en9070485

Lentz, A´., Almanza, R. (2006a). Parabolic troughs to increase the geothermal wells flow enthalpy. Sol. Energy 80, 1290e1295. https://doi.org/10.1016/ j.solener.2006.04.010.

Lentz, A´., Almanza, R. (2006b). Solar-geothermal hybrid system. Appl. Therm. Eng. 26, 1537e1544. https://doi.org/10.1016/j.applthermaleng.2005.12.008.

Leonard, L. (2023, January 16). Top 5 biggest solar farms in the U.S. Construction Review Online. https://constructionreviewonline.com/biggest-projects/top-5-biggest-solar-farms-in-the-us/

Li, K., Bian, H., Liu, C., Zhang, D., Yang, Y. (2015). Comparison of geothermal with solar and wind power generation systems. Renew. Sustain. Energy Rev. 42, 1464e1474. https://doi.org/10.1016/j.rser.2014.10.049.

Li, M., & Lior, N. (2015, July 1). Analysis of Hydraulic Fracturing and Reservoir Performance in Enhanced Geothermal Systems. Journal of Energy Resources Technology, 137(4). https://doi.org/10.1115/1.4030111

Liang, F., Sayed, M., Al-Muntasheri, G. A., Chang, F. F., & Li, L. (2016, March). A comprehensive review on proppant technologies. Petroleum, 2(1), 26–39. https://doi.org/10.1016/j.petlm.2015.11.001

Mathur, P.N. (1979). An Assessment of Solar-Geothermal Hybrid System Concepts.Department of Energy.

McClure, M., Kang, C., & Fowler, G. (2022, January 25). Optimization and Design of Next-Generation Geothermal Systems Created by Multistage Hydraulic Fracturing. Day 1 Tue, February 01, 2022. https://doi.org/10.2118/209186-ms

McTigue, D. J. P., Zhu, G., Turchi, C. S., Mungas, G., Kramer, N., King, J., & Castro, J. (2018, June 5). Hybridizing a Geothermal Plant with Solar and Thermal Energy Storage to Enhance Power Generation. https://www.osti.gov/biblio/1452695/

Menges, C.M. and McFadden, L.D. (1981). Evidence for a latest Miocene to Pliocene transition from Basin-Range tectonic to post-tectonic landscape evolution in southeastern Arizona: Tucson, Arizona Geologic Society Digest 13, p. 151-160.

Michaelides, E. E. (2018). Energy, the Environment, and Sustainability (Mechanical and Aerospace Engineering Series) (1st ed.). CRC Press.

National Solar Database. (2022). SEIA. https://www.seia.org/national-solar-database

N.C. Clean Energy Technology Center. (2017). DSIRE, Energy Efficiency Standards, Arizona

NC Clean Energy Technology Center. (2018). DSIRE, Arizona Renewable Energy Standard

NC Clean Energy Technology Center. (2021). DSIRE, Net Billing, Arizona

Nebraska Energy Office. (August 2022). Comparison of Solar Power Potential by State, accessed September 4, 2022.

Nielsen, K.W., Børgesen, J. (2012). Geothermal heat pump combined with a hybrid solar energy system. http://proceedings.dtu.dk/fedora/ repository/dtu:419/OBJ/ Geothermalheatpumpcombinedwithahybridsolarenergysystem.pdf.

NREL. (2021). Concentrating Solar Power Projects by Technology. Retrieved July 23, 2022, from NREL: https://solarpaces.nrel.gov/by-technology

Qazi, S. (2017). Solar Thermal Electricity and Solar Insolation. Stand-alone Photovoltaic (P.V.) Systems for Disaster Relief and Remote Areas, 203–237. https://doi.org/10.1016/b978-0-12-803022-6.00007-1

Qi, X., Wang, J., Królczyk, G., Gardoni, P., & Li, Z. (2022). Sustainability analysis of a hybrid renewable power system with battery storage for islands application. Journal of Energy Storage, 50, 104682. https://doi.org/10.1016/j.est.2022.104682

Rai, G. D. (2023). Solar Energy Handbook. Mercury Learning & Information.

Richter, D.H., Houser, B.B., and Damon, P.E. (1983). Geologic map of the Guthrie quadrangle, Graham and Greenlee Counties, Arizona: U.S. Geological Survey Miscellaneous Investigations Series Map I-1455, scale 1:48,000.

Ruzzenenti, F., Bravi, M., Tempesti, D., Salvatici, E., Manfrida, G., Basosi, R. (2014). Evaluation of the environmental sustainability of a micro-CHP system fueled by low-temperature geothermal and solar energy. Energy Convers. Manag. 78, 611e616. https://doi.org/10.1016/j.enconman.2013.11.025.

Ryan Randazzo, The Arizona Republic. (2022, January 26). In major reversal, Arizona utility regulators kill 100% clean-energy rules in the state. Arizona Republic. https://eu.azcentral.com/story/money/business/energy/2022/01/26/arizona-corporation-commission-votes-down-carbon-free-energy-rules-3-2/9227048002/

Schwarz, D. H. (December 27, 2021). The fastest growing states in the U.S. are all out West, Deseret News

Selover, N. (2022). Arizona-A State of Mild Temperatures as well as Extremes, Arizona's Climate, The CoCoRaHS 'State Climates' Series

Solar Energy Local. (2023). Solar energy and solar power in Clifton, AZ. https://www.solarenergylocal.com/states/arizona/clifton/

SolarGIS. (2015). Solar resource maps of China. https:// solargis.com/maps-and-gis-data/download/china. accessed 6.4.19.

SolarGIS. (2016). Solar resource maps of the world. https://solargis.com/maps-and-gis-data/download/world. accessed 6.4.19.

Solarific. (2023). Solar panel angles for Clifton, Arizona — Solarific. https://solarific.co/us/az/clifton

Spadacini, C., Xodo, L.G., Quaia, M. (2016). Geothermal Energy Exploitation with Organic Rankine Cycle Technologies, Organic Rankine Cycle (ORC) Power Systems: Technologies and Applications. Elsevier Ltd. https://doi.org/10.1016/B978- 0-08-100510-1.00014-4.

Spencer, J. E., Richard, S. M., Bykerk-Kauffman, A., Constenius, K. N., & Valencia, V. A. (2022). Structure, chronology, kinematics, and geodynamics of tectonic extension in the greater Catalina metamorphic core complex, southeastern Arizona, USA. Geosphere, 18(6), 1643–1678. https://doi.org/10.1130/ges02485.1

Tempesti, D., Manfrida, G., Fiaschi, D. (2012). Thermodynamic analysis of two micro-CHP systems operating with geothermal and solar energy. Appl. Energy 97, 609e617. https://doi.org/10.1016/j.apenergy.2012.02.012.

Thorman, C.H.(1981).Geology of the Pinaleno Mountains, Arizona—a preliminary report, in Stone, Claudia and Jenney, J.P., eds.: Arizona Geological Society Digest, V. 13, p. 5-11.

Tucson Electric Power. (2021, April 20). Our Steps to Sustainability. Tucson Electric Power. Retrieved August 5, 2022, from https://www.tep.com/news/our-steps-to-sustainability/

Tyagi, V. V., Kaushik, S. C., & Tyagi, S. K. (2012, January 18). Advancement in solar photovoltaic/thermal (PV/T) hybrid collector technology. Renewable and Sustainable Energy Reviews, 16, 1383-1398.

U.S. Census Bureau. (2010). Census: Arizona Profile, Population Density by Census Tract.

U.S. Census Bureau. (2019). Arizona, Table B25002, Occupancy Status, 2019 American Community Survey 1-Year Estimates, and Table B25004, Vacancy Status, 2019 American Community Survey 1-Year Estimates.

U.S. Census Bureau. (March 2011). Population Distribution and Change: 2000 to 2010, Table 1, Population Change for the United States, Regions, States, and Puerto Rico: 2000 to 2010, p. 2.

U.S. Department of Energy. (April 2006). Energy Efficiency and Renewable Energy, Geothermal Technologies Program, Arizona

U.S. EIA, State Energy Data System. (2019). Table C1, Energy Consumption Overview: Estimates by Energy Source and End-Use Sector, 2019.

U.S. EIA, State Energy Data System. (2019). Table C14, Energy Consumption Estimates per Capita by End-Use Sector, Ranked by State.

U.S. EIA. (2019). State Energy Data System, Table C1, Energy Consumption Overview: Estimates by Energy Source and End-Use Sector.

U.S. EIA. (2021). Electricity Data Browser, Net generation for all sectors, Arizona, All fuels, Conventional hydroelectric, Other renewables, Wind, All utility-scale solar, Biomass (total), All solar, Small-scale solar photovoltaic, Annual, 2001-21.

U.S. EIA. (2021). Electricity Data Browser, Net generation for all sectors, Arizona, All fuels Geothermal, Annual, 2000-21.

U.S. EIA. (February 17, 2021). Solar Explained, Solar Thermal Power Plants

U.S. EIA. (February 2022). Electric Power Monthly, Table 1.18.B.

U.S. EIA. (February 2022). Electric Power Monthly, Tables 1.17.B, 1.18.B.

U.S. EIA. (January 2022) Electricity, Preliminary Monthly Electric Generator Inventory (based on Form EIA-860M as a supplement to Form EIA-860), Inventory of Operating Generators.

U.S. EIA. (March 2022). Electric Power Monthly, Table 6.2.B

U.S.NREL. (2016). U.S. State solar resource maps https:// www.nrel.gov/gis/solar.html.

UNDESA. (2019). World Population Prospects. Department of Economic and Social Affairs. New York: United Nations. Retrieved December 2, 2022

Vollset, S. E., Goren, E., Yuan, C. W., Cao, J., Smith, A. E., Hsiao, T., Bisignano, C., Azhar, G. S., Castro, E., Chalek, J., Dolgert, A. J., Frank, T., Fukutaki, K., Hay, S. I., Lozano, R., Mokdad, A. H., Nandakumar, V., Pierce, M., Pletcher, M., . . . Murray, C. J. L. (2020). Fertility, mortality, migration, and population scenarios for 195 countries and territories from 2017 to 2100: a forecasting analysis for the Global Burden of Disease Study. The Lancet, 396(10258), 1285–1306. https://doi.org/10.1016/s0140-6736(20)30677-2

Walton, R. (2020, January 23). Arizona Public Service sets 100% clean energy target, but doesn't rule out carbon capture for gas plants. Utility Dive. https://www.utilitydive.com/news/arizona-public-service-sets-100-clean-energy-target-but-doesnt-rule-out/570870/

Wang, J. (2015). Geothermics and its Applications. Science Press, Beijing.

Western Regional Climate Center. (August 2, 2022) Climate of Arizona, Climate and Economy

WINDExchange: Wind Energy in Arizona. (2022). https://windexchange.energy.gov/states/az

Witcher, J. C. (1981). Geothermal energy potential of the Lower San Francisco River region, Arizona. Arizona Geol. Surv., Open File Report 81-7, 135 pp. + 3 enclosures.

Wynn, J.C. (1981). Complete Bouguer gravity anomaly map of the Silver City 1o x2o quadrangle, New Mexico-Arizona: Miscellaneous Investigations Series Map I-1310-A, scale 1:250,000.

Zarrouk, S. J., & Moon, H. (2014). Efficiency of geothermal power plants: A worldwide review. Geothermics, 51, 142–153. https://doi.org/10.1016/j.geothermics.2013.11.001

Zhou, C., Doroodchi, E., Moghtaderi, B., 2013. An in-depth assessment of hybrid solar-geothermal power generation. Energy Convers. Manag. 74, 88e101. https://doi.org/10.1016/j.enconman.2013.05.014.